Highlights

A Dual-Function Nonlinear Electromechanical Oscillator for Thermal Sensing and Vibration Energy Harvesting

Lucas José Dantas Alcântara, Arthur Barbosa, Rafael de Oliveira Teloli, Najib Kacem, Paulo Sérgio Varoto, Noureddine Bouhaddi

- A novel dual-function system for sensing and vibration energy harvesting;
- Experimental validation of a nonlinear thermo-electromechanical oscillator;
- Sensitivity analysis of dominant dynamic parameters in design decisions.

A Dual-Function Nonlinear Electromechanical Oscillator for Thermal Sensing and Vibration Energy Harvesting

Lucas José Dantas Alcântara[a,*], Arthur Barbosa[b], Rafael de Oliveira Teloli[b], Najib Kacem[b], Paulo Sérgio Varoto[a], Noureddine Bouhaddi[b]

[a] *Department of Mechanical Engineering, São Carlos School of Engineering, University of São Paulo, Av. Trabalhador São-carlense 400, São Carlos, 13566-590, São Paulo, Brazil*
[b] *Université Marie et Louis Pasteur, CNRS, institut FEMTO-ST, F-25000, Besançon, France*

Abstract

This paper presents the development and experimental validation of a novel nonlinear electromechanical oscillator that simultaneously enables vibration energy harvesting and thermal sensing. The originality lies in exploiting temperature-induced axial forces, arising from boundary conditions, as a mechanism to shift the system's natural frequency. Such modulation directly affects the piezoelectric transducer output, allowing the device to function as a dual-purpose structure for both sensing and energy harvesting. To characterize the three-domain multiphysics behavior, a mathematical model is developed using modal analysis and the harmonic balance method, capturing the nonlinear dynamic response with a fidelity confirmed experimentally. A sensitivity analysis reveals the key parameters that govern electrical power output, offering insights for design optimization as a function of the selected application. Beyond demonstrating the feasibility of the dual-function ap-

*Corresponding author

Email addresses: lucasjosedantas@hotmail.com (Lucas José Dantas Alcântara), arthur.barbosa@femto-st.fr (Arthur Barbosa), rafael.teloli@femto-st.fr (Rafael de Oliveira Teloli), najib.kacem@femto-st.fr (Najib Kacem), varoto@sc.usp.br (Paulo Sérgio Varoto), noureddine.bouhaddi@femto-st.fr (Noureddine Bouhaddi)

proach, the results open perspectives for active thermal load control and multiphysics extensions to other domains.

Keywords: Nonlinear multiphysics oscillations, Model parameter identification, Dual-function systems, Sensitivity analysis, Piezoelectric mechanisms, Thermally induced stresses

---

1. Introduction

Piezoelectric energy harvesters have been studied over the past two decades [1] and continue to advance, finding applications across a wide range of fields. In one of the pioneering studies in the area, Roundy and Wright [2] developed a vibration-driven piezoelectric energy generator, formulating an analytical model and validating it experimentally. Such model enabled power output estimation and laid the groundwork for design optimization of future studies. Ongoing developments have established this technology as a viable solution for several applications, including MEMS [3, 4], hearing devices [5, 6], wearable electronics [7, 8], bio-inspired systems [9, 10], railways [11, 12], wind energy harvesting [13–15], and hydraulic systems [16].

However, the effectiveness of linear vibration mechanisms strongly depends on their resonance operating conditions [17]. Dutoit et al. [18] highlighted this problem, by developing a coupled electromechanical model of a piezoelectric energy harvester, determining an optimal power condition and providing design guidelines. The frequency dependence was also observed by Erturk and Inman [19], who developed a linear model for a cantilevered bimorph piezoelectric energy harvester, accounting for different electrode connection configurations and demonstrating that performance degrades significantly when the system operates off-resonance. To overcome this limitation, researchers have introduced nonlinearities into the system, increasing the model's complexity while enabling the emergence of bifurcations, chaotic behavior, multi-stability, and bandwidth enlargement [20, 21].

Building upon on these earlier developments [18, 19], Stanton et al.

[22] investigated nonlinear effects in the electromechanical coupling of the oscillator, identifying nonlinearities even at low excitation amplitudes and emphasizing the importance of including such effects to improve modeling accuracy. Subsequent studies have further explored nonlinearities in multiple directions. For instance, Mahmoudi et al. [23] employed a hybrid piezoelectric–electromagnetic harvester to enhance both power density and frequency bandwidth, achieving improvements of 60% and 29%, respectively. Norenberg et al. [24] examined the impact of asymmetries in a nonlinear piezoelectric harvester by tilting the entire system and comparing its response to a symmetric configuration. In addition, Li et al. [25] analyzed a cantilever beam with geometric nonlinearities, adopting minimal assumptions in the derivation to construct a consistent model and evaluate common sources of error in nonlinear system formulations. Moreover, Rosso et al. [26] incorporated material nonlinearities to better capture the behavior of their harvester with intentional nonlinearities, arising from the interaction between a moving magnet and a magnetic tip mass. The same research group also recently proposed a method to manipulate the reported magnetic field [27], thereby enhancing the nonlinear effects and reporting an increase of up to seventeen times in peak power.

While most studies address intrinsic nonlinearities, discontinuous dynamics in harvester systems have also emerged as a relevant research direction. Works such as [28–30] highlight the potential of vibro-impact and stopper-based mechanisms for novel topological configurations. Among other dynamic possibilities that nonlinearities offer to energy harvesters, one could cite energy localization [31], the emergence of localized modes [32], and the exploitation of internal resonances [33]. In fact, nonlinear systems have demonstrated significant potential in distinct applications. As an example, Hermann et al. [34] introduced a novel concept for friction damping, investigated within a sandwich structure exhibiting nonlinear dynamic behavior. Furthermore, nonlinear systems have been employed for vibration control, as

shown by Barbosa et al. [35, 36], who demonstrated that introducing impurities into a chain of coupled nonlinear oscillators can lead to spontaneous soliton nucleation.

Although a large number of publications exist in the field [37, 38], the state of the art in nonlinear energy harvesters remains in active development due to its potential to power low-consumption devices [39, 40]. For instance, Xu and Zhou [41], by exploring a bistable harvester, demonstrated how the stochastic resonance of a decoupled bistable potential can be applied to bearing fault diagnosis. Still within the context of bistability, Fang et al. [42] theoretically modeled an opto-mechanical coupling system, paving a novel way for promising applications in smart structures. In the work of Sun et al. [43], the phenomenon of internal resonance was investigated by combining rotational and translational electromagnetic energy harvesters, resulting in enhanced harvesting efficiency under ultra-low-frequency excitations.

Beyond energy-focused applications, nonlinear systems have also demonstrated potential in engineering sensing technologies [44–49]. As an example, we could mention the work of Zhang et al. [47], which investigated mode localization in weakly coupled nonlinear oscillators as a means of measuring external acceleration, showing that small perturbations produce measurable variations in the oscillators' amplitudes. Research in this area has focused on leveraging nonlinear dynamics to improve the detection of subtle variations in critical physical parameters, including mass [50–56], fluid viscosity and density [57], mechanical faults [58, 59], gas [60], acoustic waves [61], flow [62] and temperature [63].

It is worth noting that the aforementioned studies are primarily directed toward specific applications; nevertheless, there is a growing interest in technologies that enable dual or multifunctional uses, particularly in nonlinear systems. In a comparative study of six generic models for dual-objective vibration mitigation and energy harvesting, Liu et al. [64] showed that electromechanical coupling not only enables energy extraction but also improves

vibration attenuation, with the extent of this benefit depending on the system architecture. The development of mechanisms that simultaneously address vibration control and energy harvesting has increasingly attracted attention from the scientific community. Recently, Wang et al. [65] introduced a piezoelectric–electromagnetic energy harvester integrated with a magnetic apparatus functioning as an energy sink. In Xu et al. [66], simultaneous vibration suppression and energy harvesting was also achieved, with particular focus on low-frequency environments. Metastructures [67], quasi-zero stiffness mechanisms [68, 69], and multi-stiffness combination strategies [70] constitute more recent examples of dual-purpose implementations in nonlinear systems, whose dynamic behaviors are considerably richer than those observed in their linear counterparts [71, 72].

Recent studies have increasingly focused on multi-physics coupling, exploring the interplay among mechanical, electrical, and thermal domains in diverse applications [73–77]. In the field of energy harvesting, multi-physics interactions have been exploited to enhance energy conversion efficiency [78, 79]. For instance, Mondal et al. [80] proposed a hybrid device integrating triboelectric and thermoelectric effects to simultaneously convert ambient mechanical and thermal energy into electricity, demonstrating the potential of multimodal energy capture. Similarly, Fadzallah et al. [81] investigated the multifunctionality of polyvinylidene fluoride, leveraging its piezoelectric and pyroelectric properties, and developed a design and optimization framework for hybrid energy harvesters.

Beyond energy harvesting, multi-physics coupling has also been investigated in other contexts [82, 83]. Mohaidat et al. [84] developed a MEMS-based electrothermal sensor for helium detection, where Joule heating induces deflections modulated by gas concentration, illustrating thermo-electromechanical coupling in sensing applications. Likewise, Yotov et al. [85] demonstrated thermal-to-mechanical-to-electrical energy conversion using shape-memory alloy wires as thermoactuators coupled with piezoelectric

elements, and further improved performance through magnetic tuning of frequency and amplitude.

Within the presented context, our work proposes a system capable of harvesting vibrational energy and detecting temperature variations through thermally induced frequency shifts. Such shifts are induced by axial forces resulting from the constrained thermal expansion of a harvester's beam, commonly studied in the literature due to its influence on natural frequency and bistability when buckled [86, 87][1]. Axial loads have been widely employed as a strategy to modify the dynamic behavior of structures, enabling the tuning of resonance frequencies to match desired operational ranges [88]. Emam and Nayfeh [89] investigated the primary resonance response of a clamped–clamped beam subjected to axial loads exceeding the critical buckling value, reporting agreement with experimental results. The study identified both qualitative and quantitative discrepancies in the static and dynamic responses, attributed to limitations of the single-mode approximation. Building upon these findings, Nayfeh and Emam [90] analyzed the vibration modes of beams with various boundary conditions and demonstrated that, beyond the first mode, equilibrium configurations tend to be unstable. The use of axial loads as a means to enhance system performance and adaptability continues to be actively explored in recent studies [91–93]. By leveraging temperature-induced axial loads, which shift the system's resonance frequency and consequently the voltage output of the transducer, our proposed system can detect the crossing of critical temperature thresholds, at which the system's natural frequency aligns with the ambient excitation frequency. Beyond the sensing capability, the same physical structure functions as a tunable energy harvester, with tuning achieved through the same physical strategy studied in [89].

A mathematical model is developed to capture the thermal effects on the

[1]One should note that beams subjected to mid-plane stretching are governed by nonlinear differential equations.

system's electromechanical behavior. Based on such model, design guidelines are proposed and experimentally validated, leading to the development of a dual-function nonlinear oscillator operating across three physical domains (mechanical, electrical, and thermal). The design process is guided by a sensitivity analysis that identifies the parameters most influential to the system's power output [94–98], and, by using the Harmonic Balance Method (HBM) [99, 100], the system's steady-state response in the frequency domain is derived. To the best of our knowledge, while prior studies have examined systems involving three physical domains [101], the integration of a multifunction perspective within this context remains scarcely addressed. By multifunctionality, particularly in the context of nonlinear dynamics, we refer to the use of a single mechanism for distinct applications, enabling structures capable of sensing, harvesting energy, and mitigating vibrations.

Temperature variations are often treated in the literature as sources of uncertainty [102, 103], increasing system variability and limiting performance. For instance, the influence of temperature on structural dynamics and energy harvesting was addressed in [104], where the effects of temperature-induced uncertainties in material properties on the dynamics of an asymmetric monostable piezoelectric energy harvester were investigated. By modeling these uncertainties stochastically, it was shown that increased thermal asymmetry amplified the voltage output, while overall uncertainty reduced efficiency. In [105], random space-dependent temperature fields were considered to induce thermal stresses that affected the natural frequencies and buckling behavior of plates. Using stochastic methods, the study demonstrated that thermal uncertainty significantly impacted structural dynamics and reliability. In [106], a data-driven method that accounted for temperature effects in vibration-based bridge damage detection was proposed. By employing neural networks, the approach successfully distinguished actual damage from temperature-induced variations, thereby reducing false alarms and improving fault localization. This work proposes to change this perspective by leverag-

ing the temperature dependence of the system to induce axial loads through restrained thermal expansion in a deterministic framework. In this context, the following contributions are presented: (i) the development of a nonlinear oscillator capable of operating in both sensing and harvesting modes; (ii) the formulation and experimental validation of a nonlinear model that incorporates multiphysics interactions, including mechanical, thermal, and electrical effects; and (iii) a sensitivity analysis that identifies the dominant dynamic parameters governing the system's electrical response, providing insight for future design strategies.

The remainder of this paper is organized as follows. Section 2 introduces the proposed system, outlining its structural characteristics and the effect of temperature variations on its natural frequency. Section 3 presents the mathematical formulation, including the modal analysis and the frequency-domain solution obtained via the HBM. Section 4 describes the experimental validation, where two experimental setups are used: an open-loop and a closed-loop configuration for controller-based tests. It is demonstrated not only the system's ability to perform its dual functionality but also its thermal-based resonance tuning capability. Finally, Section 5 summarizes the main findings and outlines potential directions for future research.

2. On the Physical Foundation of the Proposed System

This section presents the structural configuration of the proposed thermo-electromechanical system, detailing its geometry, material properties, and physical behavior. The beam assembly, including the piezoelectric patch and additional components, is described, followed by an analysis of the thermo-mechanical response resulting from constrained thermal expansion. An analytical expression is then derived to quantify the axial load induced by temperature variation. Finally, the influence of the magnet and steel plate on the system's natural frequency and its sensitivity to temperature is investigated, emphasizing their role in tuning the dynamic response and enabling

the integration of additional physical domains.

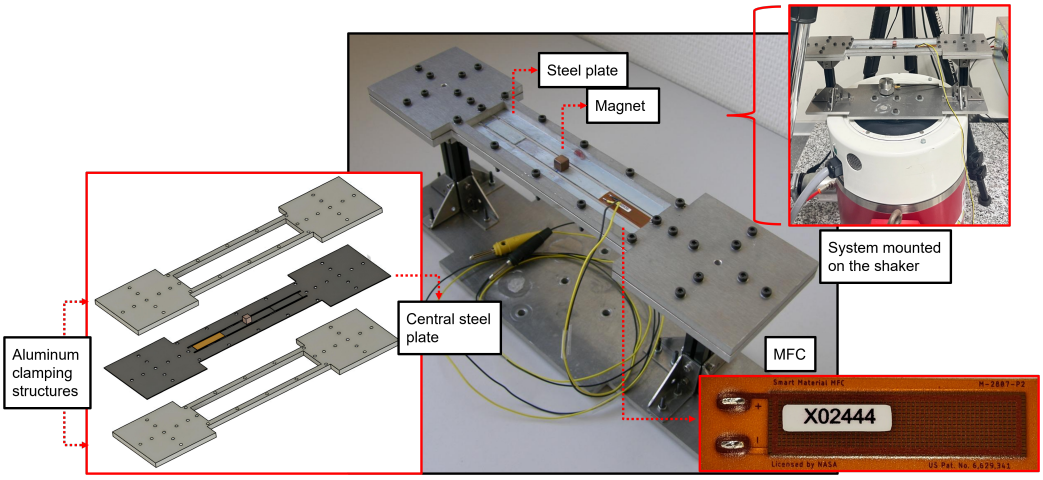

Figure 1: Physical prototype and the exploded view of the components. The main figure shows the assembled prototype, highlighting the central steel plate with the attached magnet, and the bonded MFC patch (model M2807-P2). The left side presents an exploded view of the main components, including the aluminum clamping structures, the central steel plate, and the MFC location. The right side displays the prototype mounted on the shaker. Geometric notation presented in figure 2.

The proposed system under study is illustrated in Fig. 1, which consists of two external aluminum plates enclosing a central steel plate. A beam is mounted with a magnet at its midpoint, a Macro Fiber Composite (MFC) layer at one end, and a smaller steel plate at the other. Aluminum connectors support the assembly above an aluminum base, which is coupled to a shaker to provide base excitation. Temperature variations cause thermal expansion of the structure, and due to the clamped boundaries, this elongation generates axial loads on the beam, thereby modifying its dynamic response.

A Schematic representation of the geometrical properties of the system is depicted in Fig. 2. The beam is made of steel, with a Young's modulus of $E_{steel} = 200$ GPa, density of $\rho = 7850$ kg/m^3 and a thermal expansion coefficient of $\alpha_{steel} = 12 \times 10^{-6}$ 1/°C. Its dimensions are $L \times h_s \times b = 150 \times 0.8 \times 10$ [mm], where L is the beam length, h_s its width, and b its thickness, as shown in Fig. 2. The MFC patch (M2807-P2) has a Young's modulus of

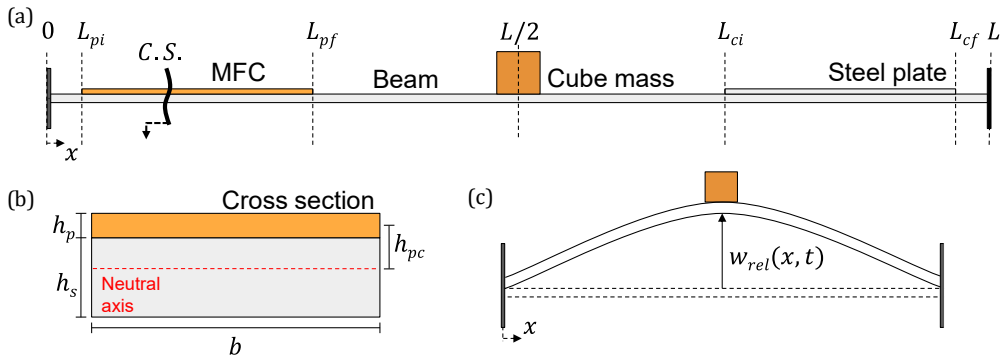

Figure 2: Schematic representation of the system. (a) Frontal view of the clamped-clamped beam indicating the total length L, the MFC patch positioned between L_{pi} and L_{pf}, the steel plate from L_{ci} to L_{cf}, and the cube mass located at $L/2$. (b) Cross-sectional view at the MFC location, showing the beam height h_s, piezoelectric patch height h_p, total height h_{pc}, and width b; the dashed red line represents the neutral axis. (c) Frontal view of the deformed beam, illustrating the transverse displacement $w_{rel}(x,t)$.

$E_p = 30.336$ GPa and dimensions $L_p \times h_p \times b = 37 \times 0.3 \times 10$ [mm], where L_p is the patch length, h_p its width, and has the same thickness as the beam. The steel plate has the same material properties as the beam and the same dimensions as the MFC. The magnet cube (343 mm^3) is made of neodymium, with a mass of $M_{conc} = 2.52$g. Finally, the clamping structure is made of aluminum, with a thermal expansion coefficient of $\alpha_{aluminum} = 23 \times 10^{-6}$ $1/°$C.

Thermal variations in the system cause expansion of its components; however, due to spatial constraints, this expansion results in axial loads on the beam. The relationship between the axial load N_T and the temperature variation ΔT is determined by considering the expansion of both the steel beam and the aluminum clamping structure, as presented in Appendix A, leading to the following equation:

$$N_T = E_{steel} A (\alpha_{aluminum} - \alpha_{steel}) \Delta T. \tag{1}$$

Since aluminum has a higher coefficient of thermal expansion than steel,

Eq. (1) indicates that temperature increases lead to tensile axial loads. Such outcome differs from previous studies [86, 87], where the thermal expansion of clamped boundaries is typically neglected, leading to a different axial load behavior. Based on the established relationship between temperature and axial loading, all subsequent analyses can be equivalently reformulated in terms of temperature variations.

The magnet and steel plate are included in the analysis due to their influence on the tuning of the natural frequency, which can be advantageous for adapting the system to varying operational requirements. Although electromagnetic energy harvesting lies beyond the scope of this study, the magnet could potentially serve that purpose, thereby enhancing the structure's energy harvesting capabilities, while also enabling the addition of an extra contribution to the system's nonlinear stiffness. Appendix B presents a simulation of natural frequency variations caused by temperature changes, examining the influence of both the magnet and the steel plate on the beam's dynamics. The results confirm the trend predicted by Eq. (1), with temperature increases leading to higher natural frequencies, consistent with the presence of tensile axial loads. The analysis further shows that the magnet decreases the resonant frequency, whereas the steel plate increases it—counteracting effects that enable frequency tuning to meet design targets. Additionally, both components reduce the sensitivity of the natural frequency to temperature variations, with the magnet exerting a more pronounced effect than the steel plate.

3. Mathematical Modeling

The current section establishes the mathematical framework used to describe the mechanism introduced in Section 2. A nonlinear beam model is developed to account for midplane stretching, thermal axial loading, and piezoelectric coupling, capturing the system's response under base excitation and temperature variation. Subsequently, the governing partial differential

equations are reduced to a low-order representation through modal decomposition, enabling both analytical and numerical evaluation of a Duffing-type equivalent oscillator. Finally, a study is conducted to evaluate the influence of axial loads on frequency domain, resulting in relations that serve as the foundation for the model calibration and sensitivity analysis conducted in the following sections.

The system is modeled as a clamped–clamped beam incorporating midplane stretching and axial load effects, with the magnet at the midpoint represented as a point mass. Static displacement due to gravity is neglected. The electromechanical coupling follows the linear piezoelectric beam model developed by Erturk and Inman [19, 107]. Nonlinear terms arising from midplane stretching and axial loading are included based on the formulation presented by Touzé et al. [108], which serves as the foundation for the mechanical model used in this study. The MFC layer is represented using equivalent piezoelectric parameters, following the approach proposed by Deraemaeker et al. [109], where a summation over representative volume elements is employed to derive the effective properties, thereby simplifying the modeling process.

3.1. Electromechanical Model

The partial differential equations (PDEs) describing the dynamics of the beam are written as follows[2]:

$$\begin{aligned}
&\frac{\partial^2}{\partial x^2}\left(EI_{eq}(x)\, w_{rel}^{xx}\right) + m(x)\,\ddot{w}_{rel} + c_a\,\dot{w}_{rel} + c_s I_s\,\dot{w}_{rel}^{xxxx} \\
&- \left(N_T + \frac{EA}{2L}\int_0^L \left(w_{rel}^{x}\right)^2 dx\right) w_{rel}^{xx} - \vartheta\left[\delta^x(x-L_{pi}) - \delta^x(x-L_{pf})\right] v(t) \\
&= -m(x)\,\ddot{w}_b,
\end{aligned} \tag{2}$$

[2]One should observe that N_T serves as a thermomechanical coupling as observed in Eq.(1).

and

$$\frac{\bar{\varepsilon}_{33}^{s} b L_p}{h_p}\,\dot{v}(t) + \frac{v(t)}{R_l} = -\bar{e}_{31} h_{pc} b \int_0^{L_p} \dot{w}_{rel}^{xx}\,dx, \tag{3}$$

where EI_{eq} is the equivalent bending stiffness (defined in Appendix C), $m(x)$ is the mass distribution along the x-axis (expressed as $\rho A + M_{conc}\delta\left(x - \frac{L}{2}\right)$) c_a and c_s are the damping coefficients due to air viscosity and structural damping, respectively, ϑ denotes the electromechanical coupling term, $\ddot{w}_b$ represents the base acceleration excitation, $H(x-d)$ is the Heaviside step function centered at $x = d$, and $\delta(x-d)$ is the Dirac delta function at the same point. As for the electrical parameters, $\bar{\varepsilon}_{33}^{s}$ is the permittivity at constant strain, R_l is the load resistance, $\bar{e}_{31}$ is the piezoelectric voltage constant, and h_{pc} is the distance from the neutral axis to the center of the piezoelectric element. Aiming to reduce the notation, when necessary, spatial derivatives are indicated by superscripts in x, e.g., w_{rel}^{x}, w_{rel}^{xx}, and w_{rel}^{xxxx}. Temporal derivatives are denoted by dots: $\dot{w}_{rel}$, $\ddot{w}_{rel}$, etc. Mixed derivatives follow the same convention, e.g., $\dot{w}_{rel}^{xx} \equiv \partial^3 w_{rel}/\partial x^2 \partial t$.

To solve the system of PDEs described by Equations (2) and (3), the beam's oscilation is represented by a series of mode shapes and modal coordinates. In this study, only the first eigenmode is considered, which allows the simplification of Eqs. (2) and (3) to a system of ordinary differential equations (ODEs) on the modal coordinate η:

$$\ddot{\eta}(t) + c\dot{\eta}(t) + k_{lin}\eta(t) + k_{nl}\eta^3(t) + \theta v(t) = \gamma F\cos(\omega t), \tag{4}$$

and

$$C_p\dot{v}(t) + \frac{v(t)}{R_l} = \theta\dot{\eta}(t), \tag{5}$$

where the complete mathematical expressions for the physical parameters are described in Appendix C [3].

[3] Appendix C presents the expression for the equivalent bending stiffness and for the

3.2. Mode Shape Analysis

The system's mode shape is determined using a modal basis from the linear, uncoupled[4] and undamped case. The resulting ODE describing the mode shape of a clamped-clamped beam under axial loads, with a lumped mass at its midpoint, is given by:

$$\overline{EI}_{eq}\frac{d^4\phi(x)}{dx^4} - N_T\frac{d^2\phi(x)}{dx^2} - \omega^2 m(x)\phi(x) = 0, \tag{6}$$

where, $\overline{EI}_{eq}$ is the mean value of the equivalent bending stiffness EI_{eq} and, for our particular case, given the clamped-clamped scenario:

$$\phi(0) = 0, \quad \phi(L) = 0, \quad \left.\frac{d\phi(x)}{dx}\right|_{x=0} = 0, \quad \text{and} \quad \left.\frac{d\phi(x)}{dx}\right|_{x=L} = 0. \tag{7}$$

We should note that continuity condition of the displacement field must also be considered at the concentrated mass: $\phi\left(\frac{L^-}{2}\right) = \phi\left(\frac{L^+}{2}\right)$. The analytical solution for the mode shape is described in Appendix D[5] and is given by the following relation:

$$\begin{aligned}\phi(x) = \frac{1}{C^2 + D^2}\big[&- \mu k^4 \phi\left(\tfrac{L}{2}\right) f\left(x - \tfrac{L}{2}\right) H\left(x - \tfrac{L}{2}\right) \\ &- \phi^{xxx}(0) f(x) - \phi^{xx}(0) f^x(x)\big],\end{aligned} \tag{8}$$

where $f(x)$ is an auxiliary function defined as:

$$f(x) = \frac{\sin(Dx)}{D} - \frac{\sinh(Cx)}{C}, \tag{9}$$

equivalent dynamic parameters obtained via modal expansion.

[4]In nonlinear regimes, mode shapes may become coupled across different frequencies. In this study, we assume the dominance of the first mode and, therefore, adopt a single-mode expansion.

[5]Appendix D presents a detailed derivation of the mode shape ODE solution.

and the wavenumber k, N_{adm}, μ, C and D are additional parameters defined as:

$$k^4 = \frac{\omega^2 \rho A}{\overline{EI}_{eq}}, \quad N_{adm} = -\frac{N_T}{\overline{EI}_{eq}}, \quad \mu = \frac{M_{conc}}{\rho A},$$

$$C = \left(-\frac{N_{adm}}{2} + \left(\frac{N_{adm}^2}{4} + k^4 \right)^{0.5} \right)^{0.5}, \tag{10}$$

$$\text{and } D = \left(\frac{N_{adm}}{2} + \left(\frac{N_{adm}^2}{4} + k^4 \right)^{0.5} \right)^{0.5}.$$

The eigenvalues associated with the employed modal basis are obtained from the determinant of the matrix Λ, defined as follows:

$$\Lambda = \frac{1}{C^2 + D^2} \begin{bmatrix} C^2 + D^2 & f^x\left(\frac{L}{2}\right) & f\left(\frac{L}{2}\right) \\ \mu k^4 f\left(\frac{L}{2}\right) & f^x(L) & f(L) \\ \mu k^4 f^x\left(\frac{L}{2}\right) & f^{xx}(L) & f^x(L) \end{bmatrix}. \tag{11}$$

Details regarding the algebraic procedure are also provided in Appendix D. It is worth noting that the influence of N_T appears explicitly in the modal base Equation (8) and in its associated matrix Λ through the variables C and D, which contrasts with some previous studies that analyzed beams under axial loads [110, 111].

By setting the determinant of the matrix in Eq.(11) to zero, the natural frequencies of the system can be obtained for different values of axial load. For the clamped-clamped beam configuration, this procedure leads to a transcendental equation, which does not admit a closed-form analytical solution; therefore, the frequencies must be computed numerically. For comparison, Appendix E presents an analytical derivation of the relationship between

natural frequency and axial load for the simply supported case, where a closed-form solution is obtained.

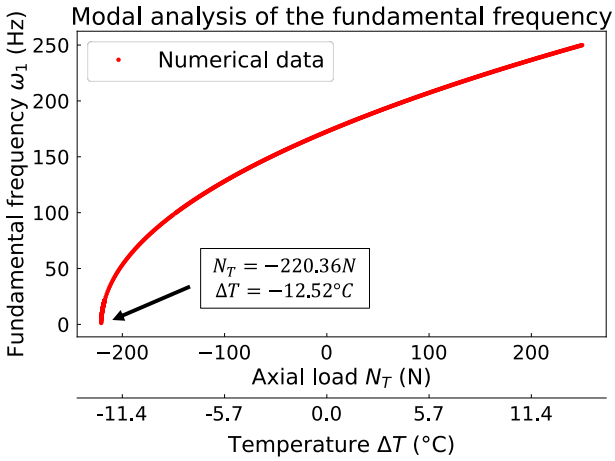

Figure 3: Fundamental frequency as a function of axial load, with the corresponding temperature variation shown on the secondary x-axis (obtained through the mode shape equations). The critical axial load and its equivalent temperature (at which the frequency tends to zero) are highlighted.

Fig. 3 illustrates the increase in the fundamental frequency under tensile axial loads and its decrease under compressive loads, eventually reaching the critical buckling load N_{cr}. The analytical expression for the critical buckling load of a clamped-clamped beam is established in the literature [90, 112] and is given by:

$$N_{cr} = \frac{4\pi^2 EI}{L^2}. \tag{12}$$

When substituting the parameters associated with our beam into Eq. (12), a critical load of $N_{cr} = -220.37$ N is obtained, which aligns with the modal analysis presented in Fig. 3, where the critical load obtained is $N_{cr} = -220.36$ N, revealing good agreement between Λ and the results reported in the literature.

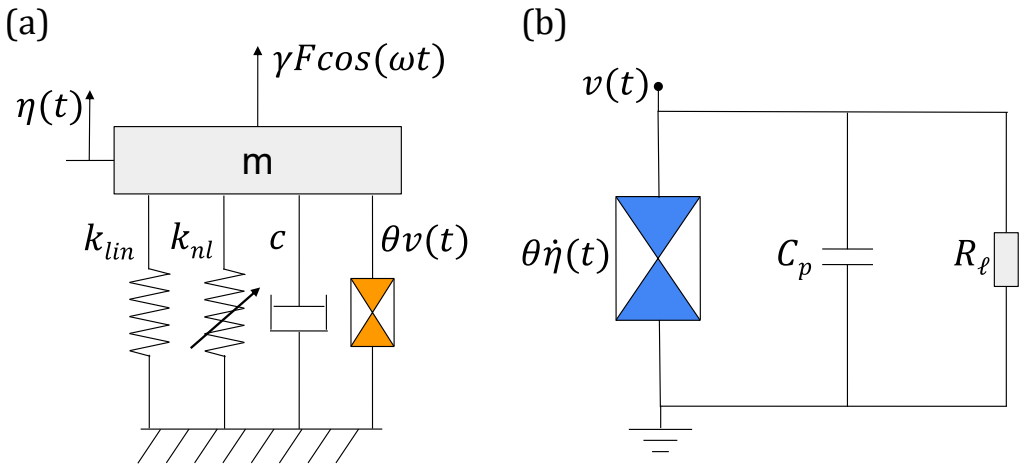

Figure 4: The equivalent system of Eqs. (4) and (5), where the inertial element m of the mechanical system is unitary in the derived equations. In a), the mechanical system is shown, and in b), the electrical system. Inertial force resulting from base acceleration is treated in its equivalent form, that is, as an external force applied to the lumped-parameter equivalent system.

3.3. Model Response in the Frequency Domain

Equations (4) and (5) describe the system's response in terms of modal coordinates and voltage and its corresponding lumped-parameter representation is illustrated in Fig. 4. The modal and physical displacements are related through the mode shape, which, at the midpoint of the beam, where the experimental measurement is taken, defines their relationship as:

$$z(t) = \phi\left(\frac{L}{2}\right)\eta(t), \tag{13}$$

with $z(t)$ being the physical displacement at $\frac{L}{2}$. Eq.(8) provides the mode shape expression, from which its value at $\frac{L}{2}$ can be obtained, enabling conversion between the two quantities. The mode shape exhibits negligible variation around $\frac{L}{2}$ for different values of N_T, and is therefore treated as constant, with $\phi\left(\frac{L}{2}\right) = 12.7$. Such approach establishes a connection between the modal

displacement used in the analytical model and the physical displacement measured in the experiments.

To simplify the algebraic treatment, Eqs. (4) and (5) are nondimensionalized. By defining the following nondimensional parameters:

$$y = \frac{\eta}{\eta_0}, \quad \eta_0 = \frac{\gamma F}{k_{lin}}, \quad \omega_n = \sqrt{k_{lin}}, \qquad \zeta = \frac{c}{2\omega_n}, \qquad \Omega = \frac{\omega}{\omega_n},$$

$$\tau = \omega_n t, \quad \alpha = \frac{k_{nl}\eta_0^2}{k_{lin}}, \qquad \upsilon = \frac{C_p \bar{v}}{\theta \eta_0}, \qquad \beta = \frac{1}{R_l C_p \omega_n}, \quad \text{and } \kappa^2 = \frac{\theta^2}{k_{lin} C_p}, \tag{14}$$

Eqs. (4) and (5) are rewritten as:

$$\frac{d^2y}{d\tau^2} + 2\zeta\frac{dy}{d\tau} + y + \alpha y^3 + \kappa^2 \upsilon = \cos(\Omega\tau), \tag{15}$$

for the mechanical domain, and

$$\frac{d\upsilon}{d\tau} + \beta\upsilon = \frac{dy}{d\tau}, \tag{16}$$

for the electrical one.

To determine the system's response in the frequency domain, the HBM is employed [16]. Accordingly, the solutions of Eqs.(15) and (16) are assumed to be harmonic, leading to expressions that relate the amplitudes of the mechanical (Y) and electrical (V) responses to the excitation frequency (Ω), by means of:

$$\left(A_6 Y^6 + A_4 Y^4 + A_2 Y^2 - 1\right) = 0, \tag{17}$$

and

$$V^2 = \frac{Y^2\Omega^2}{\Omega^2 + \beta^2}, \tag{18}$$

where

$$
\begin{aligned}
A_6 &= \frac{9\alpha^2}{16}, \\
A_4 &= \frac{3\alpha}{2}\left(1 - \Omega^2 + \frac{\kappa^2\Omega^2}{\Omega^2 + \beta^2}\right), \\
&\text{and} \\
A_2 &= (1-\Omega^2)^2 + 4\zeta^2\Omega^2 + \frac{\Omega^2\kappa^2\left(2 - 2\Omega^2 + 4\zeta\beta + \kappa^2\right)}{\Omega^2 + \beta^2}.
\end{aligned}
\tag{19}
$$

Equations (17) and (18) define the system's frequency response. In particular, Eq. (17) is a cubic polynomial in Y^2, potentially yielding up to three real solutions for a given excitation frequency, which are obtained numerically over the frequency range associated with the response curve. The resulting solutions are used to support both parameter identification, through a model fitting approach, and the evaluation of parameter influence, via a sensitivity analysis.

4. Experimental Campaigns and Model Validation

The present section provides the experimental procedures carried out to characterize the thermo-electromechanical behavior of the system and the validation of the mathematical model developed in Section 3. The experimental campaign is organized into two main categories based on the temperature control strategy: open-loop and closed-loop conditions. The experimental setup is described for both conditions, including the instrumentation used for measuring mechanical, electrical, and thermal responses under controlled conditions. These tests are performed to evaluate the system's behavior across varying temperatures, excitation frequencies, and electrical load values. Subsequently, a model fitting procedure is implemented using Particle Swarm Optimization (PSO) in order to calibrate the model parameters against experimental data for the particular case of the open-loop configura-

tion [6]. The identified trends and parameter sensitivity are then discussed to assess the model's predictive capabilities and alignment with physical observations.

4.1. Open-Loop Temperature Control

4.1.1. Experimental setup

The experimental apparatus used in the open-loop series of tests is illustrated in Fig. 5. The setup is mounted on the shaker table of a Data Physics V100 system, driven by a DSA5K-1 power amplifier. The input acceleration is measured by a DJB A/600 accelerometer, fixed on the flat surface of the base. Meanwhile, the electrical voltage generated by the MFC is recorded, and the velocity at the center of the beam is monitored using an Ometron VH300+ laser vibrometer. The infrared thermal imager Optris XI400 is employed for non-contact temperature monitoring of the beam during the experiments. According to the manufacturer's specifications, the system accuracy is $\pm 2\,^{\circ}\mathrm{C}$ of the reading at ambient conditions, which limits its performance in terms of absolute temperature acquisition. Nevertheless, the camera provides a high thermal sensitivity of 80 mK (0.08 °C), allowing it to reliably detect small relative variations in temperature. In practice, once the initial reference temperature is calibrated, the system captures relative changes with a precision on the order of $10^{-2}\,^{\circ}\mathrm{C}$. Such characteristic makes the device particularly suitable for the present study, since the focus is on tracking frequency-temperature relationships and relative thermal fluctuations rather than on the absolute temperature of the structure. All signals are acquired and processed through an M+P International VibPilotE spectral analyzer and subsequently stored on two computers for further analysis.

The heating in the experiments is provided by an electric convection heater (Bionaire BFH3520, digital tower fan heater, rated power 2400 W).

[6] The experimental setup associated with the closed-loop configuration is used exclusively to verify the thermal tuning and repeatability of the mechanism's response.

The device operates with a built-in thermostat and automatic cycling, progressively raising the air temperature until the setpoint of 35 °C is reached on its terminal. The heater is positioned at approximately 1 m from the test structure, acting as a controlled heat source, while the actual temperature control and monitoring are applied directly on the beam. Such choice avoids uncertainties caused by the additional heat generated by auxiliary equipment (shaker, amplifier, computers), which increases the room temperature but not uniformly the structure. Owing to the steel's high thermal conductivity and small thickness of the beam, gradients are neglected [113]. Although we do not specify a heating rate, the experimental protocol ensures that the controlled variable is the average temperature of the beam's surface area, which remains stable during the tests when the heat source is turned off.

As shown in Fig. 6, the arrows indicate the direction of the electrical signal flow throughout the system. The excitation signal, generated by the acquisition board, is amplified and applied to the testbench. Simultaneously, acceleration is measured at the base of the structure and used as a reference input to compute the electromechanical FRs. The voltage signal produced by the MFC passes through a resistance decade box, allowing adjustment of the load resistance over a wide range (1 Ω to 10 MΩ). In parallel, a thermal camera monitors the system's temperature by periodically transmitting infrared images of the beam to an auxiliary computer.

Fig. 7 shows the initial temperature condition of the assembled system. Since the assembly is performed at 20.2°C, this state is defined as the undeformed reference configuration. The clamping structure is fastened to the beam using M3 bolts tightened to a torque of 1 Nm. Such torque, relatively high for M3 threads, ensures that the experimental setup behaves as a rigid, monolithic structure. A similar condition was adopted in the work of Teloli et al.[114], where M4 bolts spaced at 30 mm guaranteed monolithic behavior under dynamic excitation. In the present setup, bolt spacing ranges from 15 mm to 40 mm, with a higher torque applied, thus justifying the no-slip

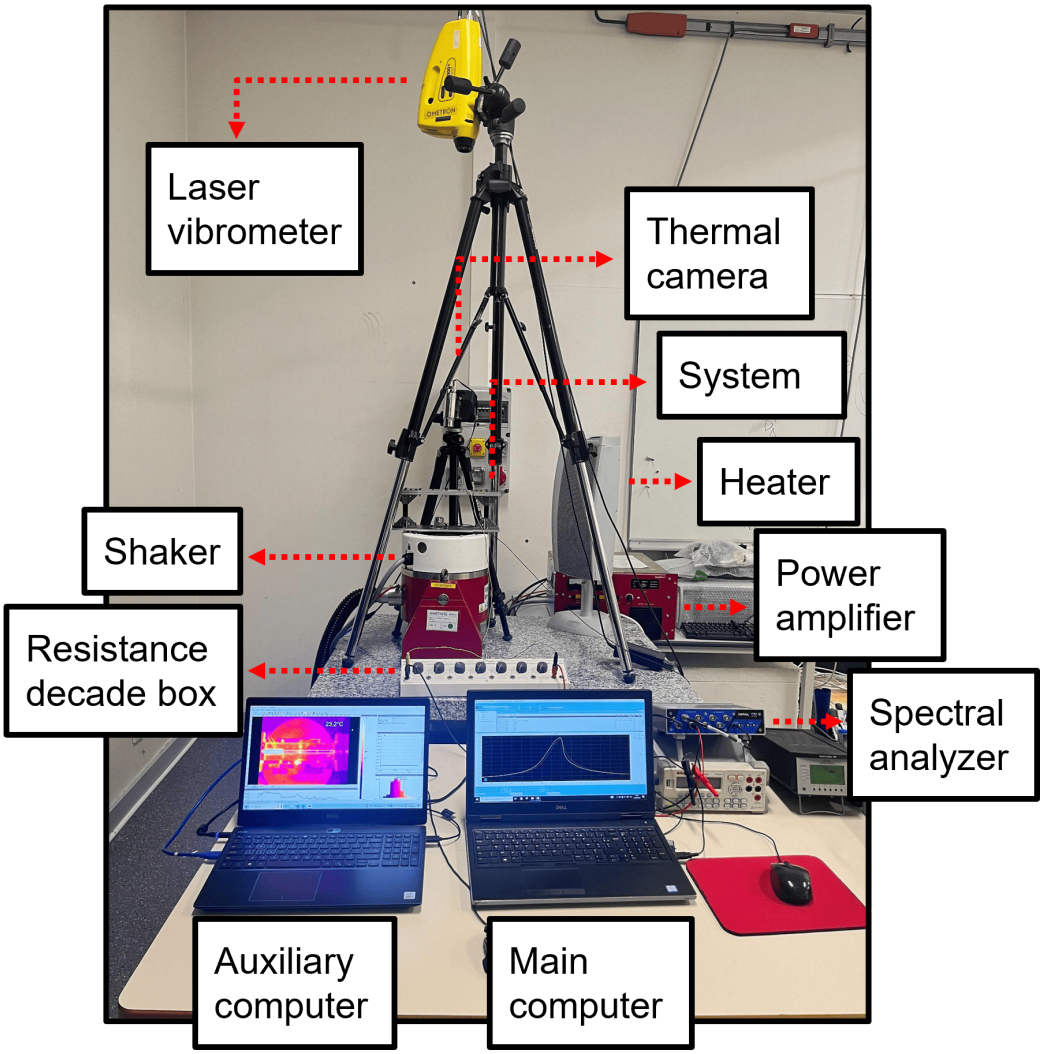

Figure 5: Overview of the experimental setup, indicating the components involved in the measurements and data post-treatment. Temperature increase occurs either gradually, due to heat accumulation from equipment operating in a closed environment, or abruptly, via an external heater. Likewise, cooling takes place progressively after testing is interrupted or with a higher rate when assisted by compressed air.

assumption.

The experimental campaign under open-loop temperature control begins with frequency-domain analyses conducted at various temperatures under

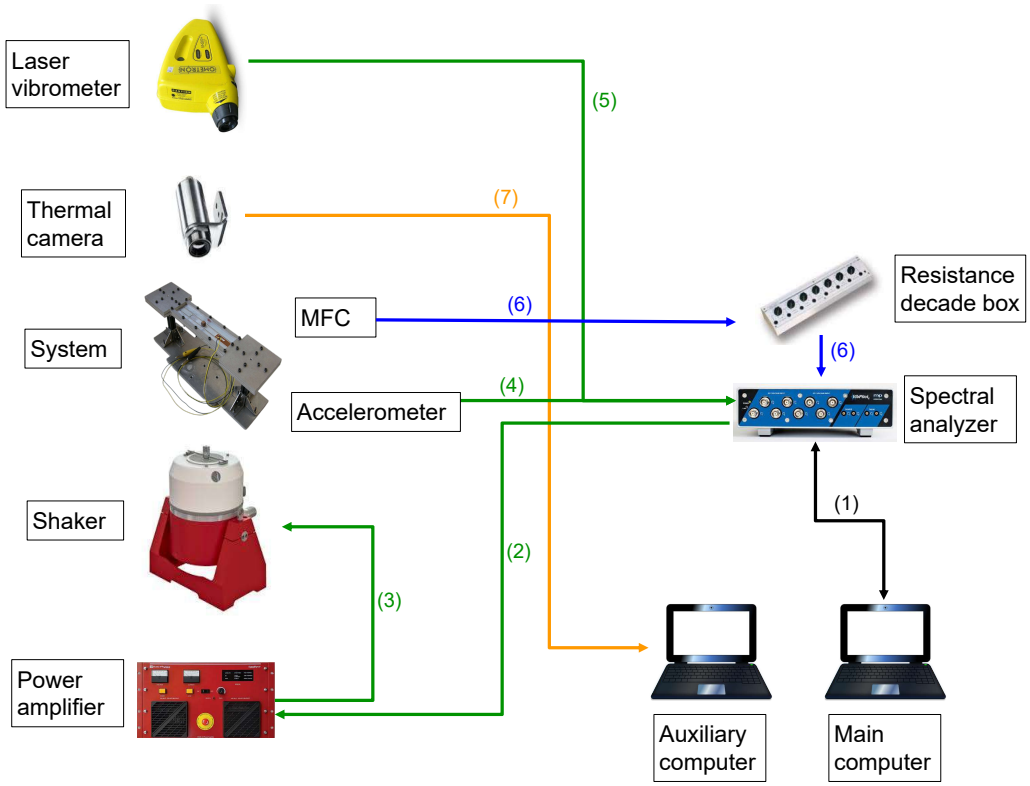

Figure 6: Diagram of the experimental setup. The arrow colors represent signals from different physical domains: green for mechanical quantities, blue for electrical quantities, and orange for thermal ones.

closed-circuit conditions, with constant electrical resistance. In the first set of tests, the system is analyzed at a fixed temperature, with the heater turned off during measurements. After recording the frequency response, heating is applied, when necessary, to gradually raise the ambient temperature to the next target level. This procedure enables the identification of correlations between system parameters and thermal variations. In the second series of experiments, the system is excited at a fixed frequency while the temperature is progressively increased by continuous heating of the surrounding environment. Such controlled procedure allows the observation of the system's response near a critical temperature, where a sudden increase in volt-

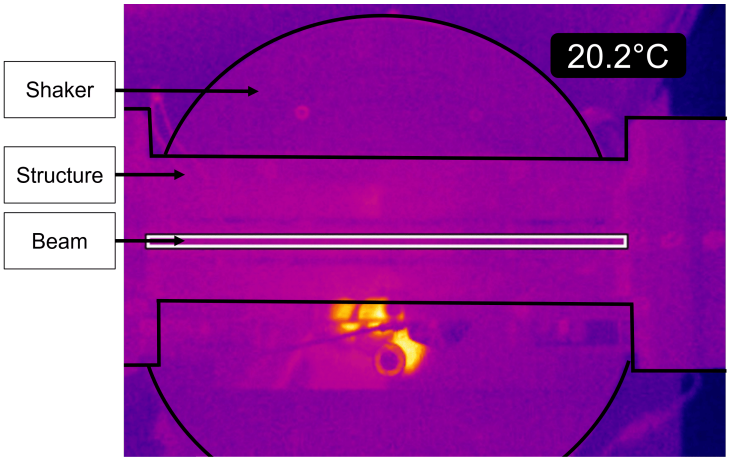

Figure 7: Thermal image of the system during assembly, with contour and labels indicating the shaker, structure, and beam. The interior white rectangle marks the area where the average temperature is calculated (value shown in the upper right corner).

age is detected. Additionally, a third set of tests is performed at constant temperature in order to investigate the effect of the electrical resistance on the system's output. In such case, the excitation frequency is kept constant and the resistance is varied parametrically across a wide range, allowing the identification of the R value that maximizes power output, crucial in VEH application.

4.1.2. Model Fitting

The model fitting is performed using a Particle Swarm Optimization (PSO) algorithm to fit the parameters of the mathematical model presented in Eqs. (4) and (5) to the experimental data. By using the frequency response expressions in Eqs. (17) and (18), the model may yield up to three solutions at a given excitation frequency, two stable and one unstable branch. However, only the upper stable branch is considered, as it corresponds to the highest critical amplitudes observed experimentally.

Before performing the parameter fitting process, a sensitivity analysis is conducted to identify which parameters most significantly affect the sys-

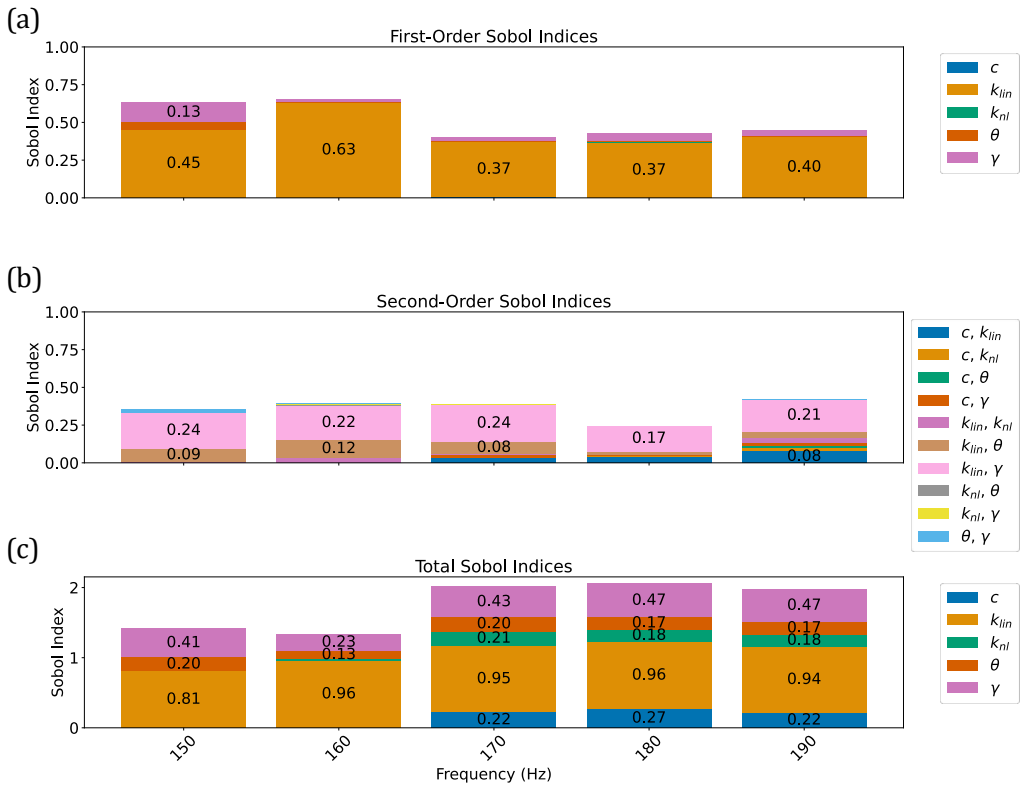

Figure 8: First-order, second-order, and total Sobol indices for different excitation frequencies. (a) First-order indices showing the individual contribution of each parameter. (b) Second-order indices representing pairwise interactions between parameters. (c) Total Sobol indices accounting for both individual and interaction effects. Parameters analyzed: damping c, linear stiffness k_{lin}, nonlinear stiffness k_{nl}, electromechanical coupling θ, and modal force γ.

tem's output. The input vector is defined as $\mathbf{X} = c, k_{\text{lin}}, k_{\text{nl}}, \theta, \gamma$, encompassing damping, linear and nonlinear stiffness, electromechanical coupling, and modal force. The analysis is carried out across a range of excitation frequencies to assess parameter influence under typical operating conditions.

Recalling Equation (18), the electrical power amplitude is given by:

$$P_0 = \frac{\theta^2 z_0^2}{C_p^2 R_l} V^2, \tag{20}$$

which is used as the objective function in the sensitivity analysis presented in Fig. 8. The first-order Sobol indices show that k_{lin} has the highest individual influence on the output power. The second-order indices further indicate a strong interaction between k_{lin} and γ, suggesting that their combined effect is also significant. This result is confirmed by the total Sobol indices, which identify k_{lin} and γ as the dominant contributors to the output variability.

Based on this result, the variations of the parameters k_{nl}, c, and θ can be considered to have negligible influence under the tested conditions and are therefore assumed constant across different temperatures during the model fitting process. Conversely, only k_{lin} and γ are treated as temperature-dependent and are adjusted to match experimental data. Such choice is supported by their dominant influence on the system's response: k_{lin} directly affects ω_n, determining how close the system operates to resonance for a given excitation frequency, which strongly impacts the output power. Similarly, γ reflects the amplitude of the external excitation force, also governing the energy transferred into the system. As both parameters directly shape the system's dynamic behavior and electrical response, their identification across temperature variations is essential for accurately describing and predicting the system's performance.

Based on the results of the sensitivity analysis, which identified k_{lin} and γ as the dominant parameters influencing the system's output, the optimization process focuses on adjusting only these two parameters while keeping c, k_{nl}, and θ fixed. The goal is to minimize the discrepancy between the model predictions and the experimental data. The objective function $J(k_{lin}, \gamma)$ is defined as:

$$J(k_{lin}, \gamma) = \sum_{i=1}^{N} \left[\tilde{e}_i^{\text{mec}} + \tilde{e}_i^{\text{ele}} \right], \tag{21}$$

where $\tilde{e}_i^{\text{mec}}$ and $\tilde{e}_i^{\text{ele}}$ are the normalized error terms, defined as:

$$\tilde{e}_i^{\text{mec}} = \frac{e_i^{\text{mec}} + 1.25\chi_{1,i}^{\text{mec}} e_i^{\text{mec}} + 1.5\chi_{2,i}^{\text{mec}} e_i^{\text{mec}}}{\max\limits_j \left(e_j^{\text{mec}} + 1.25\chi_{1,j}^{\text{mec}} e_j^{\text{mec}} + 1.5\chi_{2,j}^{\text{mec}} e_j^{\text{mec}}\right)}, \tag{22}$$

associated with the mechanical domain, and

$$\tilde{e}_i^{\text{ele}} = \frac{e_i^{\text{ele}} + 1.25\chi_{1,i}^{\text{ele}} e_i^{\text{ele}} + 1.5\chi_{2,i}^{\text{ele}} e_i^{\text{ele}}}{\max\limits_j \left(e_j^{\text{ele}} + 1.25\chi_{1,j}^{\text{ele}} e_j^{\text{ele}} + 1.5\chi_{2,j}^{\text{ele}} e_j^{\text{ele}}\right)}, \tag{23}$$

associated with the electrical one, where:

$$e_i^{\text{mec}} = \left(y_i^{\text{mec}} - \hat{y}_i^{\text{mec}}\right)^2, \quad \text{and} \quad e_i^{\text{ele}} = \left(y_i^{\text{ele}} - \hat{y}_i^{\text{ele}}\right)^2. \tag{24}$$

The variables y_i^{mec}, $\hat{y}_i^{\text{mec}}$, y_i^{ele}, and $\hat{y}_i^{\text{ele}}$ correspond to the measured and estimated mechanical and electrical responses at frequency f_i. The indicator functions used to define the frequency-weighted windows are given by:

$$\begin{aligned} \chi_{1,i}^{\text{mec}} &= \begin{cases} 1, & \text{if } |f_i - f_{\max}^{\text{mec}}| \leq 1.5 \text{ Hz} \\ 0, & \text{otherwise} \end{cases}, \\ \chi_{2,i}^{\text{mec}} &= \begin{cases} 1, & \text{if } |f_i - f_{\max}^{\text{mec}}| \leq 0.5 \text{ Hz} \\ 0, & \text{otherwise} \end{cases}, \end{aligned} \tag{25}$$

and

$$\begin{aligned} \chi_{1,i}^{\text{ele}} &= \begin{cases} 1, & \text{if } |f_i - f_{\max}^{\text{ele}}| \leq 1.5 \text{ Hz} \\ 0, & \text{otherwise} \end{cases}, \\ \chi_{2,i}^{\text{ele}} &= \begin{cases} 1, & \text{if } |f_i - f_{\max}^{\text{ele}}| \leq 0.5 \text{ Hz} \\ 0, & \text{otherwise} \end{cases}, \end{aligned} \tag{26}$$

where $f_{\max}^{\text{mec}}$ and $f_{\max}^{\text{ele}}$ denote the frequencies at which the maximum measured amplitudes of the mechanical and electrical responses occur, respectively.

The function $J(k_{lin}, \gamma)$ in Eq. (21) is built on a normalized quadratic error metric, enhanced with frequency-dependent weights to increase sensitivity around regions of maximum response. Specifically, two weighting windows

are introduced near the peak amplitude frequencies: one spanning ±1.5 Hz, weighted by 1.25, and another narrower window of ±0.5 Hz, weighted by 1.5.

The experimental data used for the optimization process are obtained as described in subsection 4.1. The PSO algorithm is configured to run for a maximum of 80 iterations, with a stopping criterion that terminates the search if the improvement in the best-found solution falls below 10^{-8}. The swarm consists of 100 particles and the parameter limits are defined through an iterative procedure: first, a initial adjustment is performed to estimate the order of magnitude of each parameter, from which search intervals are established. The starting points of the parameters is guided by their influence on the response curves: the resonant frequency defines the order of magnitude of k_{lin}; the damping coefficient c and the nonlinear stiffness k_{nl} shape the slope and amplitude of the backbone curve; the parameter θ sets the relative amplitudes of the mechanical and electrical responses; and γ controls the overall response amplitude. For our system, the initial search interval is $k_{lin} = [1{\times}10^6,\ 2{\times}10^6]$, $\gamma = [0.1,\ 0.5]$. In subsequent experiments, the optimal values obtained from the previous iteration are used as reference points, and new bounds are set within ±20% of those values, under the assumption that experimental variations should not significantly alter the system parameters.

4.1.3. Model Validation

In order to validate the model, ten fits are performed using the PSO algorithm with different seeds to ensure repeatability. The fitted results show no significant differences (dispersion rate of k_{lin}: 0.013% and γ: 0.34%), indicating the consistency of the optimization strategy. A table presenting the mean values and standard deviations of the ten fits is provided in Appendix F. Fig. 9 (a) and (b) show the evolution of the identified parameters k_{lin} and γ as functions of temperature, obtained through the fitting of the experimental frequency response curves. Both parameters exhibit a clear increasing trend with temperature, reflecting the system's stiffening behavior. Points (1–4) in Fig. 9(c) illustrate representative cases where the fitted model

is compared with experimental sweep-up and sweep-down curves. The fitted results show good agreement with the measurements, accurately capturing the frequency shift induced by temperature variations. It should be noted that this first experimental campaign aims to verify the Duffing model in its ability to describe the dynamic behavior over a temperature variation range.

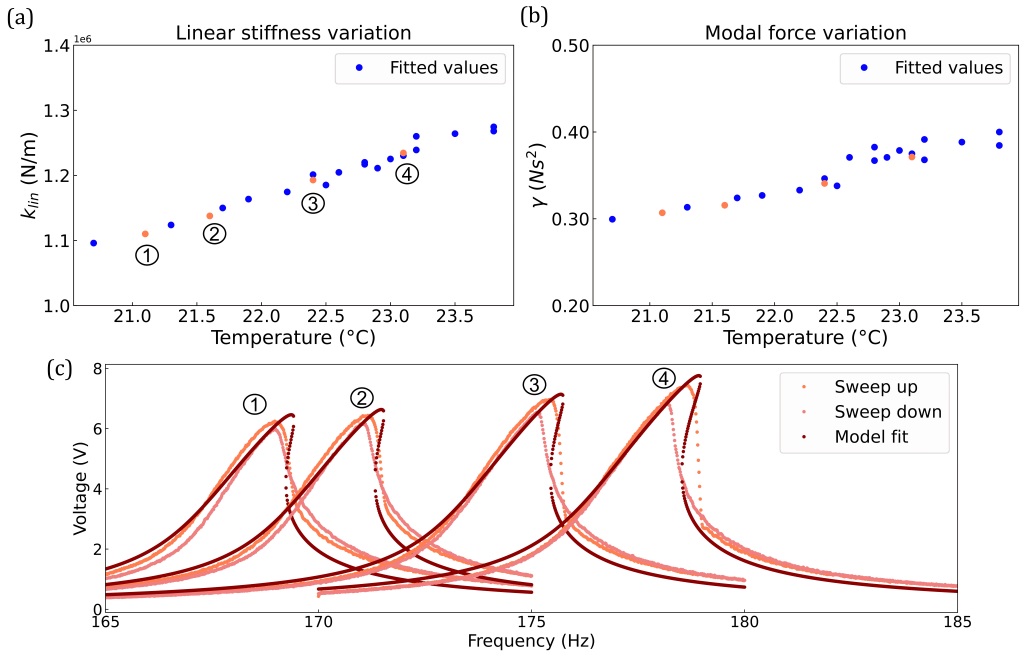

Figure 9: Parameter identification and model validation under thermal variation. (a) Identified values of the linear stiffness k_{lin} as a function of temperature, showing a monotonic increase. (b) Identified values of the modal force γ under the same conditions, also increasing with temperature. (c) Frequency response curves obtained experimentally and from the fitted model for selected temperature conditions (1–4). The model accurately captures the amplitude and shift in resonance behavior in both sweep-up and sweep-down directions.

To further validate the developed model, two parametric analyses are carried out by varying the system's external acceleration (see Fig. 10) and electrical load resistance (see Fig. 11). These tests aim to assess the model's ability to predict the frequency response (both in the mechanical and electrical domains) using experimental data not employed during the fitting process.

As can be seen in the figures, the model accurately represents the system's behavior under changes in excitation and electrical boundary conditions.

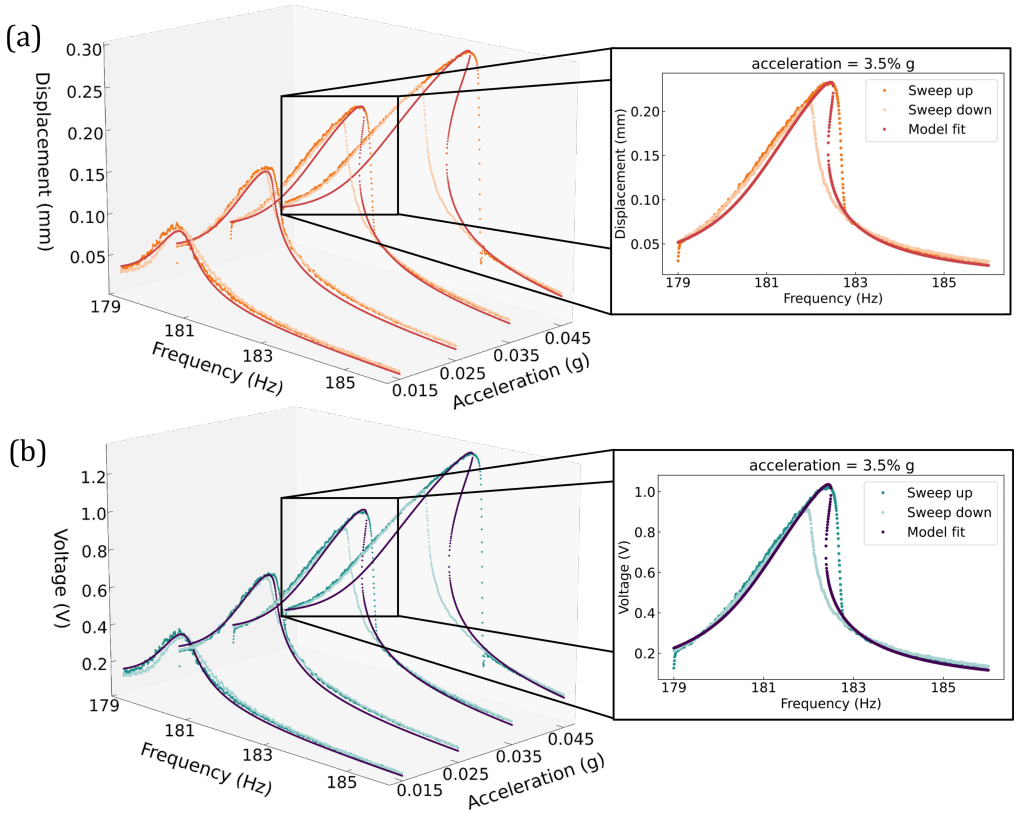

Figure 10: Parametric analysis of the system's response under varying excitation accelerations. (a) Mechanical displacement and (b) electrical voltage are shown as functions of frequency and excitation amplitude. Light colors represent experimental data for sweep-up and sweep-down tests, while dark colors correspond to the fitted model responses. The insets highlight the agreement between model and experimental data at an excitation level of 3.5% g, demonstrating the model's accuracy in capturing the system behavior across a range of operating conditions.

4.1.4. On the Harvesting Function

In energy harvesting applications, it is crucial to identify the system parameters that most significantly influence the power output, in order to maximize the energy extracted from the system. In the electrical domain, for

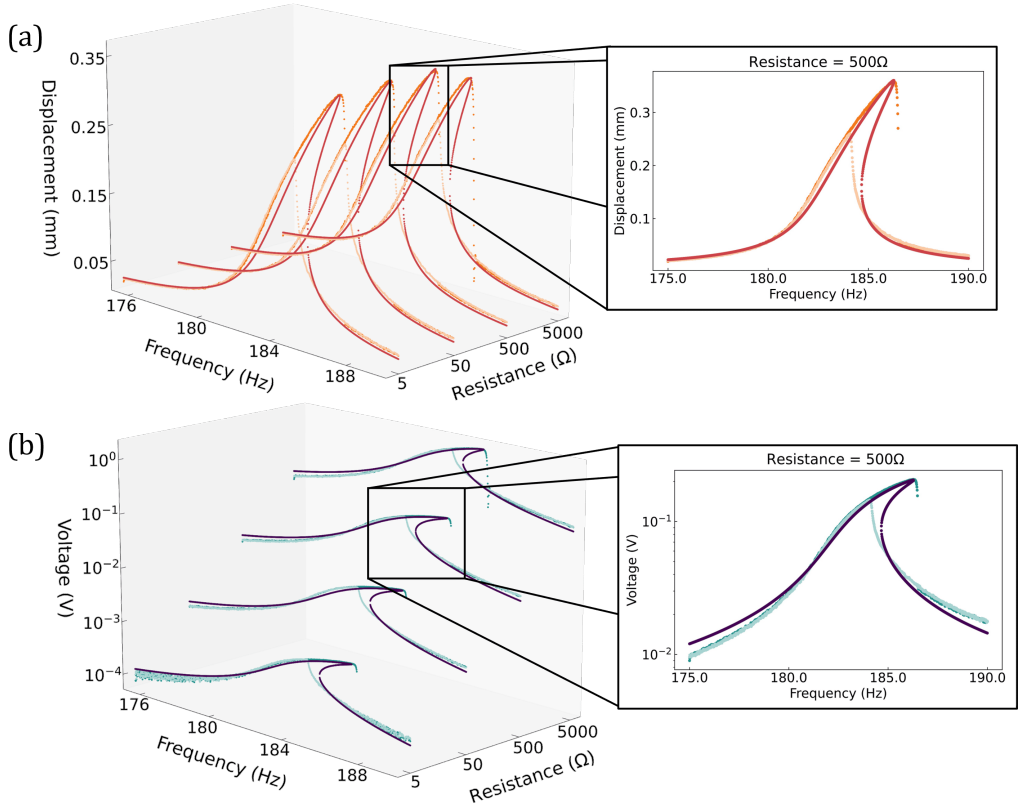

Figure 11: Parametric analysis of the system's response under varying electrical resistance. (a) Mechanical displacement and (b) electrical voltage are shown as functions of frequency and electrical resistance. Light colors represent experimental data for sweep-up and sweep-down tests, while dark colors correspond to the fitted model responses. The insets highlight the agreement between model and experimental data at an electrical load of 500 Ω, demonstrating the model's accuracy in capturing the system behavior across a range of operating conditions.

the system under study, the parameter that enables such tunability is the electrical load resistance. Fig. 12(a) shows the parametric variation of the electrical output (in terms of voltage and power) as a function of R_l, based on the model described by Eqs.(17) and (18). The model predictions are consistent with the experimental results presented in Fig. 12(b).

As shown in Fig. 12(c), increasing R_l drives the system toward an open-circuit condition, which leads to voltage saturation across the piezoelectric

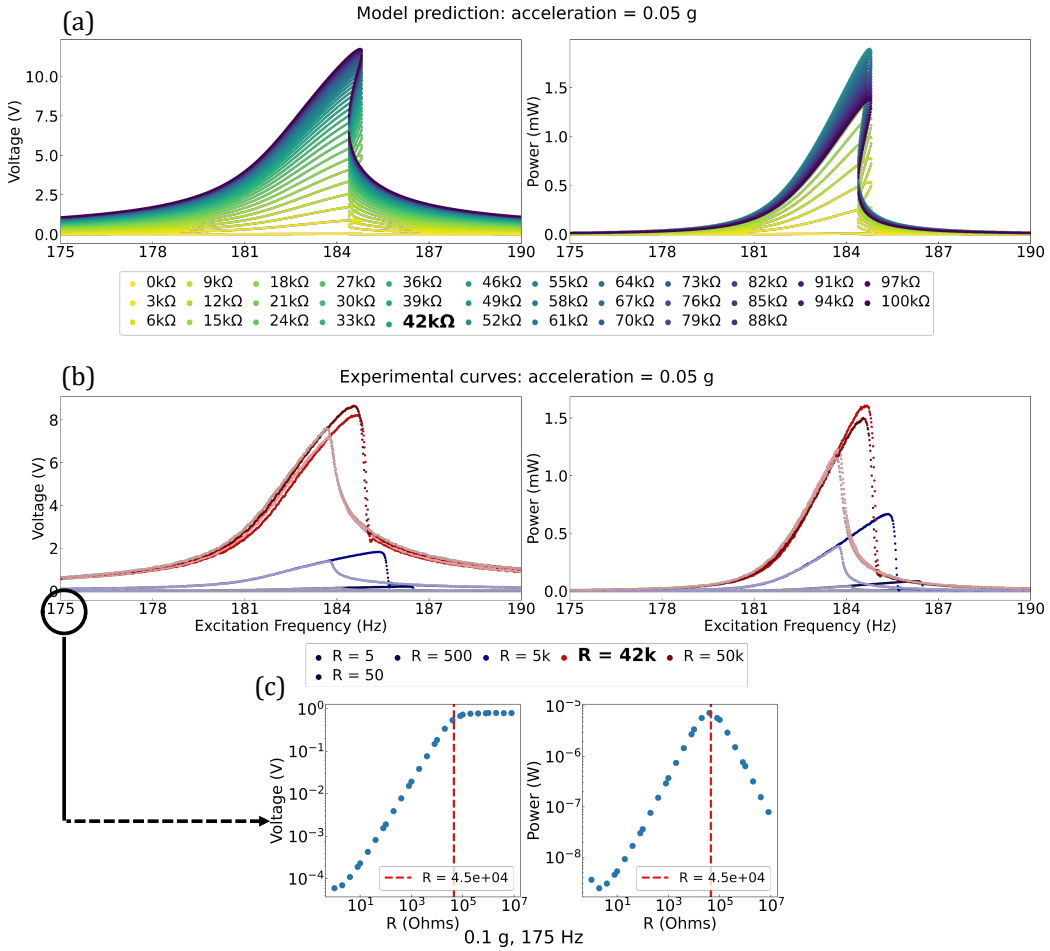

Figure 12: Investigation of the influence of load resistance on output voltage and power. In a), the Model predictions obtained from the analytical formulation; in b), the experimental measurements of voltage and power; in c), voltage and power amplitudes as functions of load resistance at a fixed excitation frequency of 175 Hz. The comparison between a) and b) shows good agreement between the experimental data and the model predictions in identifying the optimal load resistance across a frequency range. Additionally, the result in c) (for a given ω value) aligns with the analytical estimate from Eq.(27), as indicated by the red dashed line.

element and, consequently, a reduction in power output. The optimal electrical load R_{otm} that maximizes power extraction for a given excitation frequency has been analytically derived by Xiao et al. [16] for a Duffing-type

oscillator and is expressed by the following equation:

$$R_{otm} = \frac{1}{C_p \omega}. \tag{27}$$

The red dotted line in Fig. 12(c) represents the R_{otm} computed value using Eq.(27) (for $\omega = 175$ Hz), showing good agreement with the experimentally identified optimal electrical load. In fact, the analytical R_{otm} (experimentally validated in [16]) also agrees with the results across the entire simulated bandwidth in Fig. Fig. 12(a). In particular, around the resonance frequency (184.5 Hz), Eq. (27) prescribes an optimal resistance of approximately 43 kΩ, which is numerically confirmed. Experimentally, we also observe that a resistance close to this value delivers the maximum harvested power, as indicated in Fig. Fig. 12(b). One may question whether stiffness nonlinearities affect the validity of this formula; however, its derivation is related to the impedance matching between the piezoelectric element and the external circuit [115, 116], not to the resonance condition of the mechanical subsystem. Such idea relies on the assumption of the piezoelectric element operating as a current source, which remains valid as long as the resistance change does not significantly affect the transducer. Actually, Eq. (27), as well as the validation in [16], has also been corroborated in several works on nonlinear vibration energy harvesters [117–119].

Recalling the sensitivity analysis in Fig. 8, the output power is primarily governed by the linear stiffness k_{lin} and the modal force amplitude γ. Tuning k_{lin} to match the natural frequency with the excitation enhances resonance energy conversion efficiency, while increasing γ amplifies mechanical displacement, thereby boosting electrical output. Optimizing these two parameters is thus critical for maximizing harvester performance. It should also be observed that the temperature in the harvesting function is kept constant; variations in T would lead to a decrease in power output.

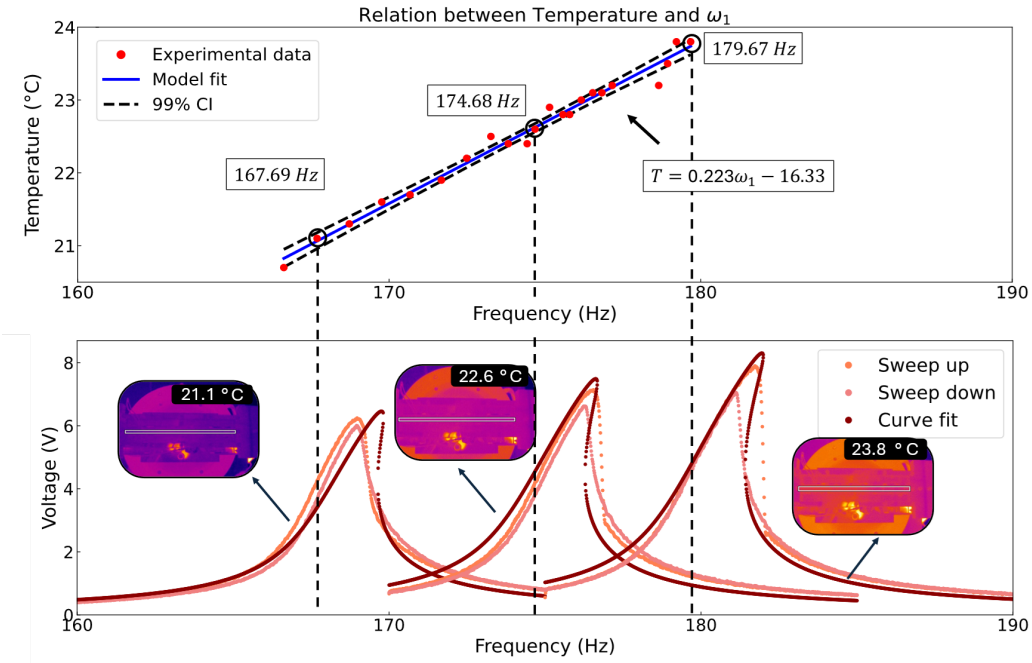

Figure 13: Relation between the system's natural frequency and temperature. In the top panel, the temperature values associated with each identified frequency are shown, along with a least squares fit used to establish an empirical relation between the natural frequency ω_1 and temperature. Dashed lines around the line fit represent a confidence interval of 99%. In the bottom panel, experimental voltage response curves (sweep-up and sweep-down) are presented for different temperatures, along with the fitted model curves. The overlaid curves show the predicted response overlaid with the actual experimental responses, demonstrating that the model is able to predict the behavior of the system.

4.1.5. On the Sensing Function

In sensing applications, understanding how temperature affects the system's natural frequency is essential, as this relationship enables the prediction of its dynamic response under specific thermal conditions. Since no closed expression directly relates the fundamental frequency to temperature variations in the clamped-clamped configuration, a numerical strategy is adopted. A functional dependence between frequency and temperature is assumed, denoted as $\omega_1 = f(T)$, to which a Taylor series expansion can be applied and fitted to the experimental data. By truncating the expansion at the first-

order term, such relationship can be approximated as linear correlation, as illustrated in Fig. 13. According with the experimental data, the approximation is valid within the temperature range considered in the present study, where variations are relatively small. However, for applications requiring higher accuracy or involving wider temperature ranges, additional terms in the Taylor expansion should be retained to improve predictive capabilities.

Fig. 13 also shows the experimental and predicted curves under varying temperature conditions, highlighting the shift in the system's resonance. Such variation enables the use of output voltage as a sensing metric for temperature variations on the order of 0.5 degrees. The dashed lines represent a 99% confidence interval, indicating a maximum prediction error of ± 0.12°C based on the fitted line over the experimental data. The sensing mechanism in this paradigm is based on the resonance condition: when the excitation frequency aligns with ω_1, the output voltage increases. Alternatively, if the excitation frequency is fixed, temperature changes gradually shift the natural frequency toward resonance.

While the sensing strategy described above detects high temperature variations through shifts in the resonant condition, bifurcations provides an alternative approach. Operating near a jumping point allows for the detection of smaller temperature increments, as slight parameter variations can trigger abrupt transitions between dynamic states, resulting in sudden voltage jumps due to branch switching in the response curve. For instance, at 24°C, a critical excitation frequency of 182 Hz can produce a sharp change of approximately 220% in output voltage within a narrow frequency interval of 0.5 Hz.

Fig. 14(a) presents a numerically simulated frequency response obtained by sweeping the excitation frequency while imposing a time-varying temperature profile, which alters the system's natural frequency. The appearance of a double peak results from a temperature decrease followed by an increase during the frequency sweep, leading the system to momentarily pass through

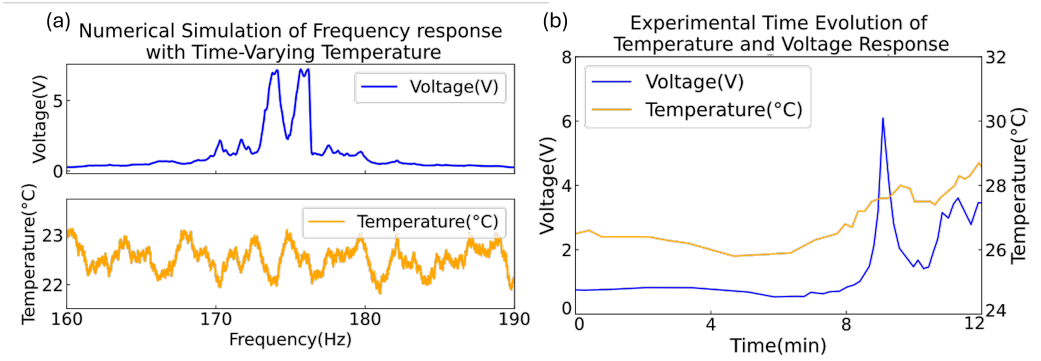

Figure 14: (a) Numerical simulation of the frequency response under a time-varying temperature profile, generated using a chirp excitation combined with the temperature curve shown below. This setup emulates thermal variations observed in experimental conditions with limited temperature control. The model incorporates the temperature influence through the empirical relation obtained in Fig. 13. The resulting double peak in the voltage response highlights the system's sensitivity to temperature changes. (b) Experimental time evolution of temperature and voltage response under a 190 Hz excitation. A sharp increase in voltage, approximately six times higher than the initial level, is observed around 8 minutes, demonstrating the system's responsiveness to thermal variations.

resonance twice. This simulation demonstrates the system's capability to detect temperature changes and suggests that it is more effective under slow thermal variations, as the system requires time to adapt its dynamic response to temperature-induced frequency shifts.

Fig. 14(b) illustrates the temperature evolution and the corresponding electrical response over time, simulating a sensing condition based on the variation of ω_1. By keeping the excitation frequency fixed at $\Omega = 190$ Hz and considering the temperature and frequency relation from Fig. 13, an estimated critical temperature of approximately 26.02°C is obtained. Experimentally, the critical temperature is observed between 26°C and 27°C, in good agreement with the predicted value. In applications where thermal switching is required, the proposed system can act as a protection mechanism, ensuring operation remains below a critical threshold.

4.2. Close-Loop Temperature Control

This section presents the validation of the proposed structure in terms of repeatability and sensitivity, while also examining the exploitation of nonlinear bifurcation phenomena for sensing applications, comparing its performance with linear regimes. The setup previously described in Section 4.1) correspond to the open-loop temperature condition, in which the beam temperature is directly measured by the thermal camera without any active temperature control. Such approach enables the characterization of the temperature influence on the system's parameters; however, it does not address aspects related to measurement repeatability or sensitivity to controlled thermal variations. For this reason, an additional set of experiments is conducted under closed-loop temperature control, allowing predefined temperature evolution profiles to be imposed and reproduced.

The experimental apparatus associated with the closed-loop control is illustrated in Fig. 15. The structure is mounted on an electrodynamic shaker (Vibration Test Systems 27 kN, TIRA), enabling base excitation. The Simcenter SCADAS Mobile system (SIEMENS) is employed for excitation control and post-processing of the measured data, while the Climats 540 H 50/3 climatic chamber provides controlled temperature conditions during testing. The temperature control is achieved by imposing a predefined profile, with the control strategy determined by the climatic chamber supplier (Climats 540 H 50/3). In this configuration, the temperature of the experiment is controlled, although the rate at which it is reached is defined by the chamber itself. Representative examples of the temperature profiles applied in the experiments are provided in Appendix G. One should note that the clamping conditions of the mechanism are specifically designed for the shaker illustrated in Figure 6, corresponding to the case with no axial loads applied to the beam. In contrast, the fixation adopted in other setups (e.g., Figure 15) uses clamps that apply compressive/tensile forces on the beam, thus modifying the resonance condition observed in the open-loop tests. Although a

frequency shift is introduced, the main objective remains the validation of the structure's repeatability and sensitivity under different thermal conditions.

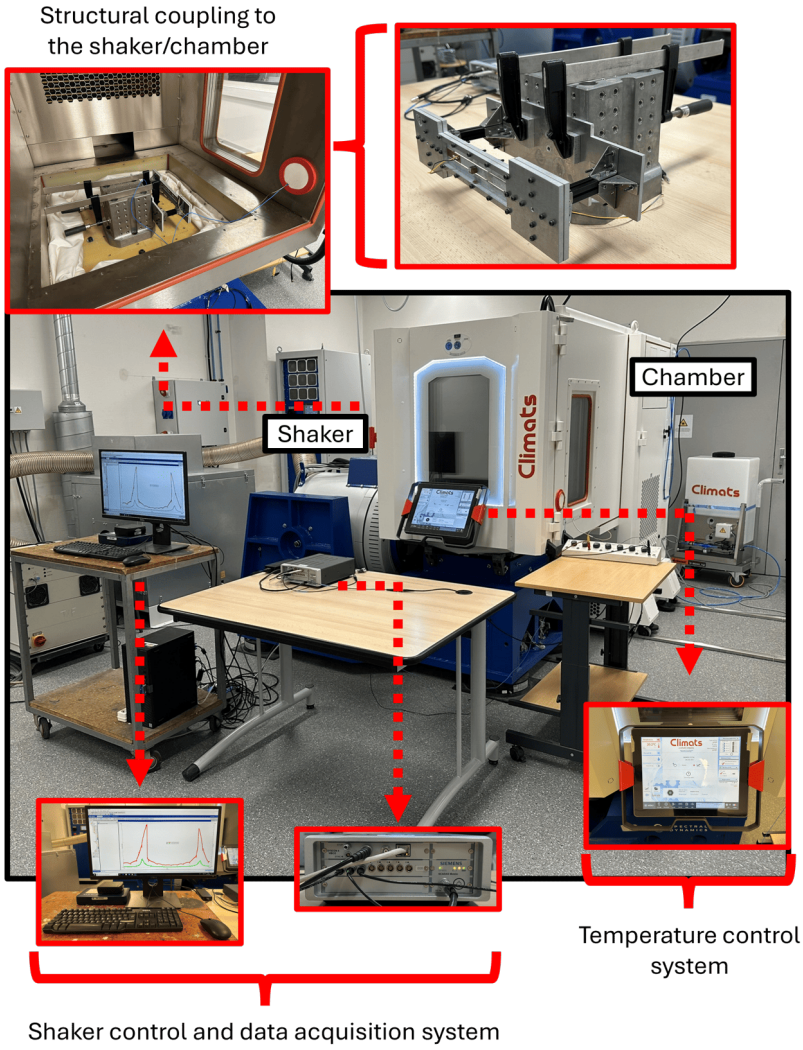

Figure 15: Experimental setup used for vibrational characterization and data acquisition under closed-loop control.

The experimental campaign under closed-loop temperature control starts with the acquisition of frequency response curves to identify bifurcation points. Then, bifurcation tests are performed by applying temperature steps

at fixed excitation frequencies to evaluate the system's transitions between stable branches. Additional tests are conducted with gradual temperature changes to assess stiffness variation, demonstrating thermo-mechanical coupling for resonance control. Finally, repeatability and sensitivity are examined by comparing frequency response curves across temperature cycles, identifying the minimum detectable variation. The temperature evolution profiles are presented in Appendix G.

4.2.1. Repeatability and Sensitivity

Fig. 16(a) shows the curves obtained for two temperature conditions, sequentially measured. The first measurements are taken at 30°C, followed by an increase to 33°C, and then a return to 30°C, repeating the procedure. It is observed that the curves corresponding to the same temperature are closely aligned, indicating that in fact the frequency response can be associated with a given temperature condition. A shift in the 30°C curves is also apparent, which may be attributed to residual stresses in the structure resulting from the heating and cooling cycles. Additionally, an increase in amplitude is observed for the 33°C curves, which is related to the effect of temperature on the structural fixations, increasing the tightening and thereby reducing overall damping. For future studies, an improvement could be done by welding the components, minimizing the influence of losses in screws and residual stresses.

Fig. 16(b) presents the curves obtained for successive temperature conditions, differing by 0.1°C. As anticipated in the sensing concept proposal, the highlighted curves confirm a temperature sensitivity on the order of 0.5 °C. One should note that branches with higher amplitudes are experimentally difficult to achieve, leading to increased deviations near the bifurcation points on the sweep-up curves. Although the mechanism exhibits high sensitivity to small temperature changes, practical measurement accuracy may be limited in the vicinity of the bifurcation.

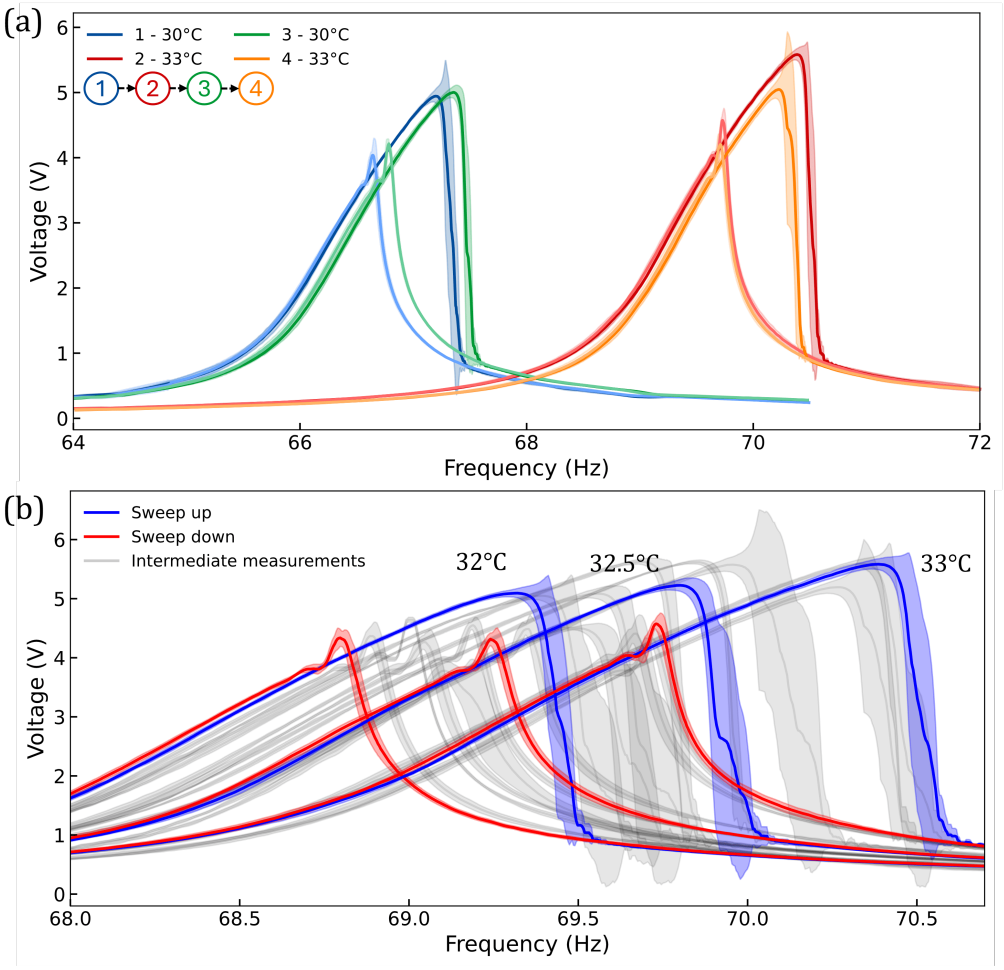

Figure 16: Validation of repeatability and sensitivity. (a) Mean response curves for two distinct temperature conditions (four curves in total). (b) Mean response curves for eleven temperature conditions, highlighting three equally spaced examples. Each mean curve is computed from 12 measurements (6 sweep-up and 6 sweep-down), with the standard deviation enveloping the curves.

4.2.2. Bifurcations

Fig. 17(a) presents the experimental frequency responses at $T = 33°\mathrm{C}$, together with the mean response curve, highlighting the frequencies at which the tests are performed. A decrease in temperature shifts the response curve to lower frequencies, causing the corresponding points to transition to the

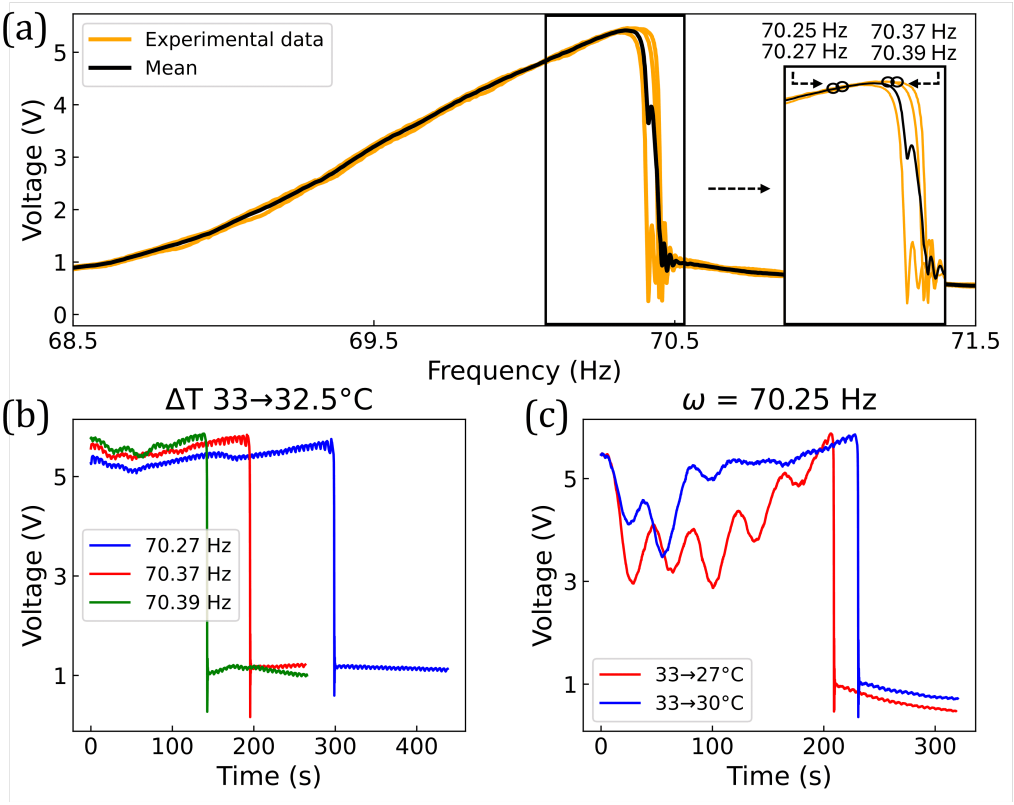

Figure 17: (a) Experimental frequency responses of the measured voltage at $T = 33°C$. Orange traces are individual experimental realizations and the black trace is the mean response; the excitation frequencies used for the time-domain tests are indicated. (b) Voltage time series for a step $\Delta T : 33 \rightarrow 32.5°C$ at three closely spaced excitation frequencies. (c) Voltage time series at fixed excitation $\omega = 70.25$Hz for two step amplitudes ($33 \rightarrow 27°C$, $33 \rightarrow 30°C$).

alternative stability branch. In line with the theory presented in Section 2, frequencies closer to the bifurcation point are expected to transition earlier toward the low-energy branches than those further away from the bifurcation, a behavior confirmed in Fig. 17(b). Following the same reasoning, for a fixed excitation frequency, a larger step input is also expected to trigger earlier jumps, which is experimentally observed in Fig. 17(c).

Fig. 18(c) shows the temperature profile applied to the system, along with the temperatures measured for both the nonlinear (high acceleration)

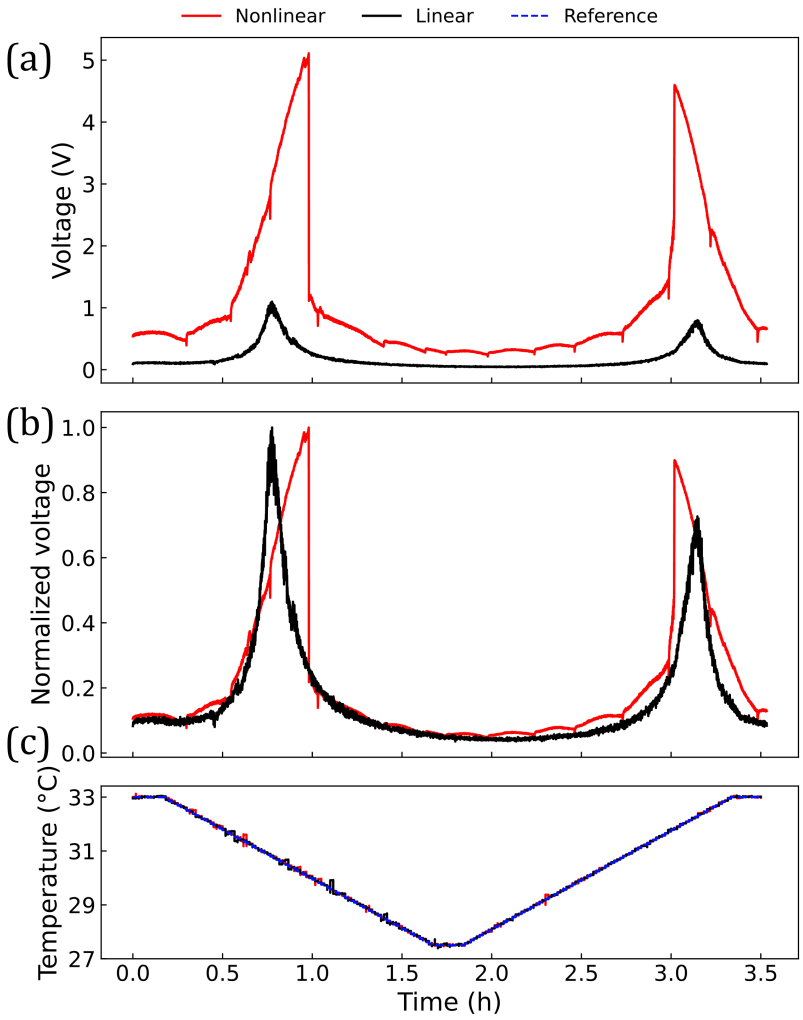

Figure 18: Temperature-controlled response of the system under linear and nonlinear regimes of oscillation. (a) Measured voltage responses for the nonlinear ($0.6g$, in red) and linear ($0.08g$, in black) excitation amplitudes. (b) Corresponding normalized voltage responses, highlighting the distinct behaviors of the two regimes. The linear response (in black) shows a gradual voltage increase near resonance, whereas the nonlinear response (in red) displays abrupt transitions associated with bifurcations. (c) Applied temperature profile (27-33°C, in blue) and measured temperatures for both configurations (in red and black).

and linear cases (lower acceleration), indicating that the system temperature closely followed the slow and uniform input. Fig. 18(b) presents the voltage measured during the experiment, normalized by the maximum value in each case (Fig. 18(a)). The nonlinear response was obtained with an excitation amplitude of 0.6g, while the linear response used 0.08g. The results demonstrate that the structure's stiffness can be thermally controlled, also showing that the nonlinear regime, due to the presence of bifurcations, exhibits higher sensitivity than the linear one. In linear conditions, the sensing mechanism is based on the resonance of the structure, resulting in a gradual voltage increase until the peak is reached. In contrast, in nonlinear conditions, bifurcations cause abrupt changes in voltage.

5. Conclusions

This paper presents the development of a nonlinear electromechanical oscillator that exhibits dual functionality, acting both as a temperature-sensitive switch/sensor and a vibration energy harvester. The system is modeled as a clamped-clamped beam with an attached MFC, under axial loads induced by temperature variations. Mismatched thermal expansion between the aluminum clamping structure and the steel beam generates tensile axial loads, increasing the system's natural frequency. A nonlinear electromechanical model is developed incorporating midplane stretching and axial load effects, with its frequency response obtained via the harmonic balance method. The model is experimentally validated using PSO-based parameter fitting, which shows that k_{lin} and γ increase with temperature, while other parameters presented a slight variation. A sensitivity analysis confirms k_{lin} and γ as the most influential parameters.

In sensing applications, the system can detect ambient temperature changes by monitoring voltage amplitudes induced by shifts in resonance. Such variations may occur gradually, as the excitation frequency sweeps through the stable branches of the Duffing oscillator. According to this

approach, large changes in ΔT are the primary target of detection. However, sensitivity can be further enhanced by leveraging the jump dynamics, wherein operation near a bifurcation point enables small parameter variations to induce abrupt transitions in the system's response. Under this alternative strategy, small values of ΔT become the focus of measurement. As a key conclusion, the sensor demonstrates a broader dynamic capability compared to linear mechanisms.

In VEH applications, the system's nonlinear nature leads to bandwidth enlargement, an advantage not attainable with single-degree-of-freedom linear systems. One should observe that the harvested power can be directly linked to thermal sensors, enabling battery-free designs or systems without external power sources. The mechanical architecture also allows tuning of ω_1 via axial loads, imposing operation near the target excitation frequency. Moreover, the presence of a central magnet introduces the potential for electromagnetic transduction, expanding the available energy conversion mechanisms, while also allowing for an additional contribution to the nonlinear stiffness of the system. Overall, as with sensing applications, the advantages of nonlinearity are retained even in simple architectures, with good agreement between experimental behavior and analytically derived optimal design parameters.

Beyond sensitivity and repeatability, the closed-loop experiments also demonstrated thermal piloting of the structural stiffness, enabling controlled transitions between stable branches through temperature modulation. Moreover, the frequency response curve is reproduced solely by varying the system temperature, demonstrating both possible jumps of the duffing oscillator (up and down sweeps). This capability reveals a new route for exploiting bifurcation-based sensing in reconfigurable structures.

In summary, the proposed structure provides a multifunctional solution for environments that demand both monitoring and energy autonomy. Its ability to adapt the frequency response via thermal loading, along with its

capacity to detect thermal shifts, highlights its potential in smart structures, embedded sensors, and energy-aware devices. Miniaturization paves the way for investigating sensing and harvesting performance at the microscale, particularly in MEMS applications. Alternatively, adaptive control strategies could be implemented to allow the system to autonomously track frequency shifts caused by temperature changes, using the MFCs as active shape modulators rather than passive elements.

Declaration of competing interest

The authors declare that they have no known competing financial interests or personal relationships that could have appeared to influence the work reported in this paper.

Acknowledgments

We gratefully acknowledge support from EUR EIPHI program, Europe (Contract No. ANR 17-EURE-0002). We also acknowledge the Bourgogne Franche-Comte region, in particular the AMETISTE platform for providing the equipments used in the closed-loop campaign.

Appendix

The following appendices provide complementary derivations, simulations, and supporting data that extend the main text. Appendix A derives the thermomechanical behavior of the structure, establishing the relation between temperature variation and the induced axial load. Appendix B presents finite element simulations that qualitatively validate this relation and illustrate the influence of structural components on thermal sensitivity. Appendix C

details the expressions for the equivalent homogenized mechanical and electrical parameters used in the reduced-order model. Appendix D provides the deduction of the analytical mode shape for the clamped–clamped configuration with a concentrated mass using Laplace transform techniques, while Appendix E derives the closed-form frequency relation for a simply supported beam under axial loading, enabling comparison with the clamped-clamped case. Finally, Appendix F compiles the experimental data obtained through parameter identification, and Appendix G exemplifies the measured temperature profiles used throughout the experimental campaign.

Appendix A. Description of the physical behavior of the system

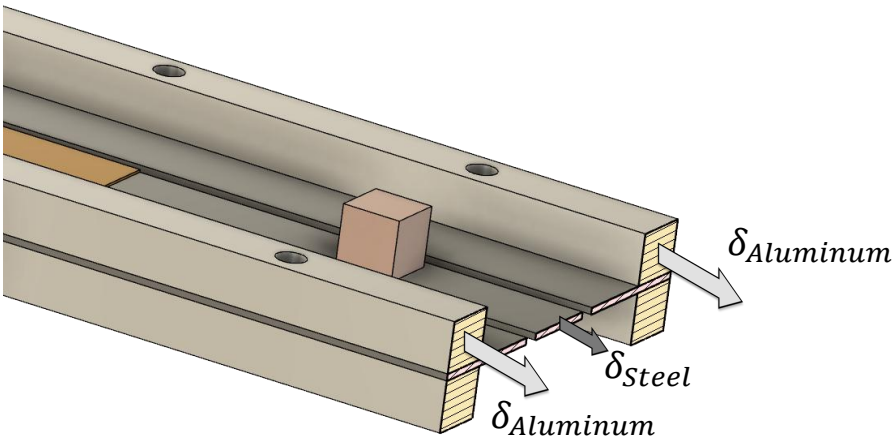

Figure A.19: Illustration of thermally induced axial deformations in the aluminum and steel components. Deformations in directions perpendicular to the beam axis are disregarded.

The structural deformation due to temperature variation is assumed to follow a linear relationship for small temperature changes, with axial deformation given by $\delta = \alpha L_0 \Delta T$, where α is the coefficient of thermal expansion

and L_0 is the initial length (thermal deformations of each component are shown in Fig. A.19). In the current configuration, both the steel beam and the aluminum clamping structures are subjected to thermal expansion. However, since aluminum exhibits a higher thermal expansion coefficient than steel, it undergoes greater elongation for the same temperature variation. One should observe that the components are mechanically assembled, consequently, constrained to deform equally, which prevents free thermal expansion and leading to the generation of internal axial forces in the beam. To quantify the axial load N_T, induced by the temperature variation ΔT, the principle of superposition is applied. The resulting axial force, obtained from the difference between the expansions, is a function of the constrained deformation, given by the Equation:

$$\delta_N = \delta_{aluminum} - \delta_{steel}, \tag{A.1}$$

so that the deformation induced by the axial force is expressed as follows:

$$\delta_N = \frac{N_T L_0}{E_{steel} A}, \tag{A.2}$$

where A is the cross sectional area of the beam. The combining of Equations (A.1) and (A.2) results in a relation between N_T and ΔT, such that:

$$N_T = E_{steel} A(\alpha_{aluminum} - \alpha_{steel})\Delta T. \tag{A.3}$$

Appendix B. Finite element simulation

Fig. B.20 presents a finite element simulation performed in COMSOL Multiphysics®, aimed at qualitatively assessing the influence of temperature on the system's natural frequency and evaluating the effects of structural modifications on its thermal sensitivity. To emphasize the general behavior rather than material-specific responses, an arbitrary piezoelectric material from the software's database is selected. The model couples thermal

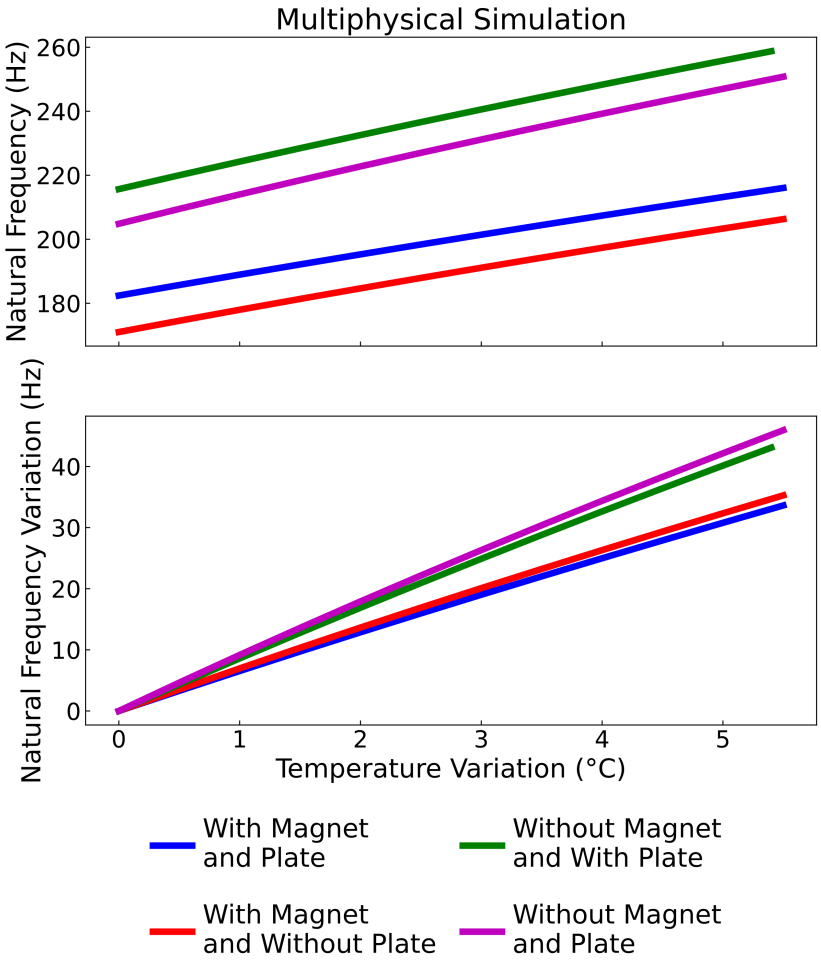

Figure B.20: Natural frequency change as a function of temperature variation obtained from COMSOL simulations. Color coding indicates the distinct configurations of the system, based on the inclusion of the magnet and/or the steel plate.

and structural physics to capture the axial loads induced by temperature variations, with eigenfrequency analyses conducted to monitor the resulting frequency shifts. A fine tetrahedral mesh with 38,672 elements ensures numerical accuracy.

The simulation results reveal a consistent increase in natural frequency with rising temperature, indicating the presence of tensile axial forces, in

agreement with the theoretical prediction from Eq. (A.3). This agreement, together with the analytical relation established in Eq. (A.3), justifies expressing all subsequent axial load effects in terms of temperature variation, allowing the incorporation of ΔT into the beam's governing equation.

To assess the system's tunability, the influence of adding a magnet at the beam's midpoint and a steel plate at its extremity is also analyzed. The inclusion of the magnet reduces the natural frequency, while the steel plate increases it, counterbalancing the magnet's effect and enabling frequency adjustment to meet specific design targets. Furthermore, the simulation shows that both components reduce the system's sensitivity to temperature-induced frequency shifts, with the magnet having a more pronounced influence. This interaction offers greater design flexibility, allowing simultaneous tuning of resonance characteristics and thermal response. Finally, it is worth noting that the magnet's presence opens the possibility of incorporating magnetic effects into the model, extending the system's applicability to a broader range of multiphysical problems.

Appendix C. Equivalent physical parameters

The equivalent bending stiffness $EI_{eq}(x)$ is given by the equation:

$$EI_{eq}(x) = \Big(E_{steel}I_s + (E_{steel}(I_{sp} - I_s) + E_pI_p)\,[H(x - L_{pi}) - H(x - L_{pf})] \\ +E_{steel}(I_{sc} - I_s)\,[H(x - L_{ci}) - H(x - L_{cf})]\Big), \tag{C.1}$$

where I_p is the area moment of inertia of the MFC, and I_{sp}, I_{sc}, and I_s represent the beam's area moments of inertia at the MFC location, the steel plate location, and all other regions, respectively. The expressions used to calculate the moments of inertia, arising from the homogenization of a composite cross section, are provided in Erturk and Inman's work [107]. It should be emphasized that EI_{eq} varies with x, and this dependence should be accounted for in the subsequent integrations. Following the modal base description, the

lumped parameters of Eqs. (4) and (5) are given by the equations:

$$
\begin{aligned}
k_{lin} &= \int_0^L \phi^{xxxx} EI_{eq}\, \phi \, dx + 2\int_0^L \phi^{xxx} EI^x_{eq}\, \phi \, dx + \int_0^L \phi^{xx} EI^{xx}_{eq}\, \phi \, dx \\
&\quad - N_T \int_0^L \phi^{xx}\, \phi \, dx, \\
k_{nl} &= -\Big(\tfrac{E_{steel}A}{2L} \int_0^L (\phi^x)^2 dx\Big) \int_0^L \phi^{xx}\, \phi \, dx, \\
c &= c_s I_s \int_0^L \phi^{xxxx}\, \phi \, dx + c_a \int_0^L \phi^2 \, dx, \\
\theta &= \vartheta\big[\phi^x(L_{pi}) - \phi^x(L_{pf})\big], \quad \gamma = -\Big(\rho A \int_0^L \phi(x)\, dx + M_{conc}\, \phi\big(\tfrac{L}{2}\big)\Big), \\
C_p &= \frac{\bar{\varepsilon}^s_{33}\, b\, L_p}{h_p}, \quad \vartheta = -\, b\, E_p\, d_{31}\, h_{pc}\,.
\end{aligned}
\tag{C.2}
$$

The parameters in Eq.(C.2) are independent of spatial variables and are treated as homogenized quantities, as they arise from an integration over the spatial domain. From the experimental perspective of this work, these parameters are determined through experimental identification.

Appendix D. Mode shape deduction

Adopting the parameter notation described in Eq.(10), Eq.(6) can be rewritten in the following format:

$$
\frac{d^4\phi(x)}{dx^4} + N_{adm}\frac{d^2\phi(x)}{dx^2} - k^4\left(1 + \mu\delta\left(x - \frac{L}{2}\right)\right)\phi(x) = 0, \tag{D.1}
$$

allowing us to apply the Laplace transform $\mathcal{L}_x$ to both sides of the Equation, in order to convert the differential equation in x into an algebraic equation in s. After applying the boundary conditions at $x = 0$ and isolating

$\mathcal{L}_x\left[\phi(x)\right](s)$, the following equation is deduced:

$$\mathcal{L}_x\left[\phi(x)\right](s) = \frac{\mu k^4 \phi\left(\frac{L}{2}\right) e^{-s\frac{L}{2}}}{s^4 + N_{adm}s^2 - k^4} + \frac{s\dfrac{d^2\phi}{dx^2}(0)}{s^4 + N_{adm}s^2 - k^4} + \frac{\dfrac{d^3\phi}{dx^3}(0)}{s^4 + N_{adm}s^2 - k^4}. \tag{D.2}$$

Before applying the inverse Laplace transform, it is convenient to rewrite the equation in a form suitable for conversion using tabulated transforms:

$$\mathcal{L}_x\left[\phi(x)\right](s) = \\ \frac{\mu k^4 \phi\left(\frac{L}{2}\right) e^{-s\frac{L}{2}}}{(s^2 - C^2)(s^2 + D^2)} + \frac{s\phi^{xx}(0)}{(s^2 - C^2)(s^2 + D^2)} + \frac{\phi^{xxx}(0)}{(s^2 - C^2)(s^2 + D^2)}. \tag{D.3}$$

Considering the relation given by:

$$\frac{1}{(s^2 - C^2)(s^2 + D^2)} = \frac{1}{(C^2 + D^2)}\left[\frac{1}{(s^2 - C^2)} - \frac{1}{(s^2 + D^2)}\right], \tag{D.4}$$

and the inverse Laplace transform properties, given by:

$$\mathcal{L}_x^{-1}\left\{s\left[\frac{1}{(s^2 - C^2)} - \frac{1}{(s^2 + D^2)}\right]\right\} = \cosh(Cx) - \cos(Dx),$$

$$\mathcal{L}_x^{-1}\left\{\left[\frac{1}{(s^2 - C^2)} - \frac{1}{(s^2 + D^2)}\right]\right\} = \frac{1}{C}\sinh(Cx) - \frac{1}{D}\sin(Dx), \tag{D.5}$$

and

$$\mathcal{L}_x^{-1}\left\{e^{-cs}U(s)\right\} = u(x - c)H(x - c),$$

the final modal expression is obtained, as shown in Equation (8).

Appendix E. Natural frequency and temperature relation for a simply supported beam

Lets assume a PDE for a simply supported beam under axial loads is given by:

$$EI\frac{\partial^4 w(x,t)}{\partial x^4} - N\frac{\partial^2 w(x,t)}{\partial x^2} + \rho A\frac{\partial^2 w(x,t)}{\partial t^2} = 0, \tag{E.1}$$

where EI is the bending stiffness, N is an axial load (positive for tensile loads and negative for compressive loads), ρ is the beam's material density and A it's cross sectional area. Under the simply supported condition, the boundary conditions are given as:

$$w(0,t) = 0, \quad w(L,t) = 0, \quad w^{xx}(0,t) = 0, \quad \text{and} \quad w^{xx}(L,t) = 0. \tag{E.2}$$

By applying the same algebraic treatment used in Appendix D, Eqs. (E.1) and (E.2) yield the following ordinary differential equation governing the mode shape:

$$EI\frac{d^4\phi(x)}{dx^4} - N\frac{d^2\phi(x)}{dx^2} - \omega^2\rho A\phi(x) = 0, \tag{E.3}$$

or, on a compact notation,

$$\frac{d^4\phi(x)}{dx^4} + N_{adm}\frac{d^2\phi(x)}{dx^2} - k^4\phi(x) = 0. \tag{E.4}$$

Still following the algebraic strategy outlined in Appendix D, the differential equation in x is transformed into an algebraic equation in s, from which the following expression is derived:

$$\mathcal{L}_x\left[\psi(x)\right](s) = \frac{\left(s^2 + N_{adm}\right)\left.\dfrac{d}{dx}\psi(x)\right|_{x=0}}{s^4 + N_{adm}s^2 - k^4} + \frac{\left.\dfrac{d^3}{dx^3}\psi(x)\right|_{x=0}}{s^4 + N_{adm}s^2 - k^4}, \tag{E.5}$$

906 or, again on a compact notation,

$$\mathcal{L}_x\left[\psi(x)\right](s) = \frac{(s^2+N_{adm})\left.\dfrac{d}{dx}\psi(x)\right|_{x=0}}{(s^2-C^2)(s^2+D^2)} + \frac{\left.\dfrac{d^3}{dx^3}\psi(x)\right|_{x=0}}{(s^2-C^2)(s^2+D^2)}. \tag{E.6}$$

907 Recalling the properties of the inverse Laplace transform, the following rela-
908 tion is finally obtained:

$$\begin{aligned}\phi(x) = \frac{1}{C^2+D^2}\Big[&\psi^{xxx}(0)\left(\frac{\sinh(Cx)}{C} - \frac{\sin(Dx)}{D}\right)\\ &+ \psi^{x}(0)\left(\left(C+\frac{N_{adm}}{C}\right)\sinh(Cx) + \left(D-\frac{N_{adm}}{D}\right)\sin(Dx)\right)\Big],\end{aligned} \tag{E.7}$$

909 where the matrix Λ associated with the eigenvalue problem under the new
910 boundary condition is given by:

$$\Lambda = \frac{1}{C^2+D^2}\begin{bmatrix} f^{xx}(L) & f(L) \\ f^{xxxx}(L) & f^{xx}(L)\end{bmatrix}, \tag{E.8}$$

911 whose determinant leads to the following relation:

$$|\Lambda| = \frac{\sin(DL)\sinh(CL)}{CD} = 0. \tag{E.9}$$

912 Since $\sinh(CL)$ is always positive for $C > 0$, the only possible solution is
913 obtained by considering $\sin(DL) = 0$, therefore, $DL = n\pi$, with $n \in \mathbf{N}^*$. By
914 enforcing the nullity through the sine condition and returning to the notation
915 associated with the physical parameters, the relationship between the natural
916 frequency and axial loads for the simply supported beam is finally derived
917 through the following equation:

$$\omega^2 = \frac{\pi^2 n^2}{\rho A L^2}\left(N + \frac{EI\pi^2 n^2}{L^2}\right). \tag{E.10}$$

From this Equation (E.10), analogously to the derivation associated with the clamped–clamped case, the first critical buckling load can be obtained by setting $\omega = 0$ and $n = 1$, yielding:

$$N_{cr} = -\frac{EI\pi^2}{L^2}. \tag{E.11}$$

Appendix F. Table of fitted data

Experimental curve	T (°C)	$\bar{k}_{lin}$ ($\times 10^6$)	$\sigma(k_{lin})$	$\bar{\gamma}$	$\sigma(\gamma)$
1	20,7	1.096	64,35	0,30	0,0005
2	21,1	1.110	87,08	0,31	0,0007
3	21,3	1.124	65,95	0,31	0,0005
4	21,6	1.138	82,83	0,32	0,0007
5	21,7	1.150	98,37	0,32	0,0008
6	21,9	1.164	71,09	0,33	0,0006
7	22,2	1.175	59,13	0,33	0,0005
8	22,5	1.185	53,53	0,34	0,0008
9	22,4	1.193	121,42	0,34	0,0009
10	22,4	1.201	161,19	0,35	0,0012
11	22,6	1.207	65,95	0,35	0,0005
12	22,9	1.213	38,37	0,35	0,0003
13	22,8	1.218	35,17	0,36	0,0003
14	22,8	1.223	67,64	0,36	0,0005
15	23,0	1.227	89,12	0,36	0,0006
16	23,1	1.232	66,81	0,36	0,0005
17	23,1	1.235	40,37	0,37	0,0003
18	23,2	1.239	47,27	0,37	0,0005
19	23,2	1.262	26,09	0,38	0,0002
20	23,5	1.265	60,83	0,38	0,0004
21	23,8	1.268	61,92	0,38	0,0004
22	23,8	1.276	71,88	0,39	0,0005

Table F.1: Parameter identification by the optimization algorithm at different temperatures T, with maximum value of dispersion rate (standard deviation over mean value) of k_{lin}: 0.013% and γ: 0.34%. The overbar notation ($\bar{\cdot}$) denotes the mean value, while the symbol σ represents the standard deviation. k_{lin} corresponds to the linear stiffness and γ to the modal force.

Appendix G. Temperature profiles

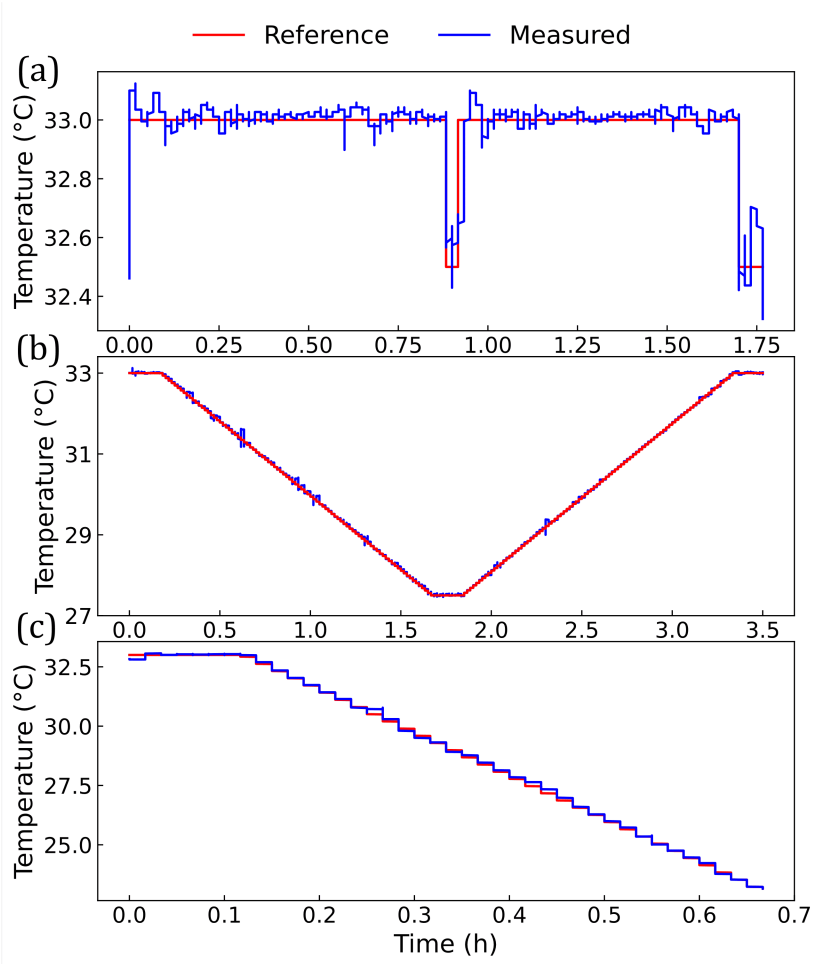

Figure G.21: Examples of experimentally imposed temperature profiles: (a) Step, (b) "V", and (c) ramp profile.

References

[1] E. L. Pradeesh, S. Udhayakumar, M. G. Vasundhara, G. K. Kalavathi, A review on piezoelectric energy harvesting, Microsystem Technologies 28 (2022) 1797–1830. URL: https://doi.org/10.1007/s00542-022-05334-4. doi:10.1007/s00542-022-05334-4.

[2] S. Roundy, P. K. Wright, A piezoelectric vibration based generator for

wireless electronics, Smart Materials and Structures 13 (2004) 1131. URL: https://dx.doi.org/10.1088/0964-1726/13/5/018. doi:10.1088/0964-1726/13/5/018.

[3] M. I. Hossain, M. S. Zahid, M. A. Chowdhury, M. M. Maruf Hossain, N. Hossain, Mems-based energy harvesting devices for low-power applications – a review, Results in Engineering 19 (2023) 101264. URL: https://www.sciencedirect.com/science/article/pii/S2590123023003912. doi:https://doi.org/10.1016/j.rineng.2023.101264.

[4] Z. Ren, C. Liu, M. Li, W. Ge, L. Zhou, H. Zhao, L. Tang, L. Ren, Comparative analysis of energy harvesting by magnetoelectric components in a simulated biological environment, International Journal of Mechanical Sciences 288 (2025) 110042. URL: https://www.sciencedirect.com/science/article/pii/S0020740325001286. doi:10.1016/j.ijmecsci.2025.110042.

[5] R. Latif, M. M. Noor, J. Yunas, A. A. Hamzah, Mechanical energy sensing and harvesting in micromachined polymer-based piezoelectric transducers for fully implanted hearing systems: A review, Polymers 13 (2021). URL: https://www.mdpi.com/2073-4360/13/14/2276. doi:10.3390/polym13142276.

[6] M. Liu, F. Qian, J. Mi, L. Zuo, Biomechanical energy harvesting for wearable and mobile devices: State-of-the-art and future directions, Applied Energy 321 (2022) 119379. doi:10.1016/j.apenergy.2022.119379.

[7] G. Singh, M. Sharma, R. Kiran, S. Karmakar, R. Vaish, Footwear for piezoelectric energy harvesting: A comprehensive review on prototypes development, applications and future prospects, Current Opinion in Solid State and Materials Science 28 (2024)

101134. URL: https://www.sciencedirect.com/science/article/pii/S1359028623000797. doi:https://doi.org/10.1016/j.cossms.2023.101134.

[8] X. Pan, G. Zhang, N. Yu, C. Cai, H. Ma, B. Yan, Low-frequency human motion energy scavenging with wearable tumbler-inspired electromagnetic energy harvesters, International Journal of Mechanical Sciences 268 (2024) 109029. URL: https://www.sciencedirect.com/science/article/pii/S0020740324000729. doi:10.1016/j.ijmecsci.2024.109029.

[9] Y. Cui, T. Yang, H. Luo, Z. Li, X. Jing, Jellyfish-inspired bistable piezoelectric-triboelectric hybrid generator for low-frequency vibration energy harvesting, International Journal of Mechanical Sciences 279 (2024) 109523. URL: https://www.sciencedirect.com/science/article/pii/S0020740324005654. doi:10.1016/j.ijmecsci.2024.109523.

[10] R. Chatterjee, C. L. Shah, S. Gupta, S. Sarkar, Energy harvesting in a flow-induced vibrating flapper with biomimetic gaits, International Journal of Mechanical Sciences 272 (2024) 109150. URL: https://www.sciencedirect.com/science/article/pii/S0020740324001929. doi:10.1016/j.ijmecsci.2024.109150.

[11] M. Bayat, I. Pakar, P. Ziehl, Nonlinear vibration of axially loaded railway track systems using analytical approach, Journal of Low Frequency Noise, Vibration and Active Control 40 (2021) 1896–1906. URL: https://doi.org/10.1177/14613484211004190. doi:10.1177/14613484211004190.

[12] J. Zuo, L. Dong, F. Yang, Z. Guo, T. Wang, L. Zuo, Energy harvesting solutions for railway transportation: A comprehensive review, Renewable Energy 202 (2023) 56–87. URL: https://www.sciencedirect.

com/science/article/pii/S096014812201641X. doi:https://doi.org/10.1016/j.renene.2022.11.008.

[13] A. Ali, S. Ali, H. Shaukat, E. Khalid, L. Behram, H. Rani, W. A. Altabey, S. A. Kouritem, M. Noori, Advancements in piezoelectric wind energy harvesting: A review, Results in Engineering 21 (2024) 101777. URL: https://www.sciencedirect.com/science/article/pii/S2590123024000306. doi:https://doi.org/10.1016/j.rineng.2024.101777.

[14] T. Tan, Z. Yan, H. Lei, W. Sun, Geometric nonlinear distributed parameter model for cantilever-beam piezoelectric energy harvesters and structural dimension analysis for galloping mode, Journal of Intelligent Material Systems and Structures 28 (2017) 3066–3078. URL: https://doi.org/10.1177/1045389X17704922. doi:10.1177/1045389X17704922.

[15] B. Tang, X. Fan, J. Wang, H. Yang, R. Bai, X. Yu, W. Tan, Energy harvesting of unequal-height cylindrical fiv considering wind direction, International Journal of Mechanical Sciences 290 (2025) 110118. URL: https://www.sciencedirect.com/science/article/pii/S0020740325002048. doi:10.1016/j.ijmecsci.2025.110118.

[16] H. Xiao, H. Qie, C. R. Bowen, Modelling of the circular edge-clamped interface of a hydraulic pressure energy harvester to determine power, efficiency and bandwidth, Mechanical Systems and Signal Processing 146 (2021) 107013. URL: https://www.sciencedirect.com/science/article/pii/S088832702030399X. doi:https://doi.org/10.1016/j.ymssp.2020.107013.

[17] B. Andò, S. Baglio, V. Marletta, A. R. Bulsara, A comparison of linear and non-linear strategies for energy harvesting from mechanical vibrations, Frontiers in Physics 10 (2023) 1032978.

[18] N. E. DUTOIT, B. L. WARDLE, S.-G. KIM, Design considerations for mems-scale piezoelectric mechanical vibration energy harvesters, Integrated Ferroelectrics 71 (2005) 121–160. URL: https://doi.org/10.1080/10584580590964574. doi:10.1080/10584580590964574. arXiv:https://doi.org/10.1080/10584580590964574.

[19] A. Erturk, D. J. Inman, An experimentally validated bimorph cantilever model for piezoelectric energy harvesting from base excitations, Smart materials and structures 18 (2009) 025009.

[20] M. F. Daqaq, R. Masana, A. Erturk, D. Dane Quinn, On the Role of Nonlinearities in Vibratory Energy Harvesting: A Critical Review and Discussion, Applied Mechanics Reviews 66 (2014) 040801. doi:10.1115/1.4026278.

[21] L. G. Costa, L. L. S. Monteiro, M. A. Savi, Multistability investigation for improved performance in a compact nonlinear energy harvester, Journal of the Brazilian Society of Mechanical Sciences and Engineering 46 (2024). doi:10.1007/s40430-024-04766-5.

[22] S. C. Stanton, A. Erturk, B. P. Mann, D. J. Inman, Nonlinear piezoelectricity in electroelastic energy harvesters: modeling and experimental identification, Journal of Applied Physics 108 (2010).

[23] S. Mahmoudi, N. Kacem, N. Bouhaddi, Enhancement of the performance of a hybrid nonlinear vibration energy harvester based on piezoelectric and electromagnetic transductions, Smart Materials and Structures 23 (2014) 075024. URL: https://dx.doi.org/10.1088/0964-1726/23/7/075024. doi:10.1088/0964-1726/23/7/075024.

[24] J. P. Norenberg, R. Luo, V. G. Lopes, J. V. L. Peterson, A. Cunha, Nonlinear dynamics of asymmetric bistable energy harvesters, International Journal of Mechanical Sciences 257

(2023) 108542. URL: https://www.sciencedirect.com/science/article/pii/S0020740323004447. doi:https://doi.org/10.1016/j.ijmecsci.2023.108542.

[25] J. Li, X. He, X. Yang, Y. Liu, A consistent geometrically nonlinear model of cantilevered piezoelectric vibration energy harvesters, Journal of Sound and Vibration 486 (2020) 115614.

[26] M. Rosso, E. Kohtanen, A. Corigliano, R. Ardito, A. Erturk, Nonlinear phenomena in magnetic plucking of piezoelectric vibration energy harvesters, Sensors and Actuators A: Physical 362 (2023) 114667. URL: https://www.sciencedirect.com/science/article/pii/S0924424723005162. doi:https://doi.org/10.1016/j.sna.2023.114667.

[27] M. Rosso, S. Cuccurullo, F. P. Perli, F. Maspero, A. Corigliano, R. Ardito, A method to enhance the nonlinear magnetic plucking for vibration energy harvesters, Meccanica 59 (2024) 1577–1592. doi:10.1007/s11012-024-01856-5.

[28] M. Wu, J. Zhang, H. Wu, Vibration mitigation and energy harvesting of vibro–impact dielectric elastomer oscillators, International Journal of Mechanical Sciences 265 (2024) 108906. doi:10.1016/j.ijmecsci.2023.108906.

[29] Y. Li, G. Zhang, S. Yao, Y. Peng, Piezoelectric-triboelectric energy harvester with elastic double-side stoppers, International Journal of Mechanical Sciences 280 (2024) 109561. doi:10.1016/j.ijmecsci.2024.109561.

[30] P. Wang, Y. Liu, R. Zhu, L. Qin, J. Deng, Z. Yang, Z. Qin, F. Chu, Dynamic analysis of vibro-impact energy harvester with acoustic black hole, International Journal of Mechanical Sciences 291–292 (2025) 110193. doi:10.1016/j.ijmecsci.2025.110193.

[31] K. Aouali, N. Kacem, N. Bouhaddi, E. Mrabet, M. Haddar, Efficient broadband vibration energy harvesting based on tuned non-linearity and energy localization, Smart Materials and Structures 29 (2020) 10LT01. doi:10.1088/1361-665X/abaa95.

[32] K. Aouali, N. Kacem, N. Bouhaddi, M. Haddar, On the optimization of a multimodal electromagnetic vibration energy harvester using mode localization and nonlinear dynamics, Actuators 10 (2021). URL: https://www.mdpi.com/2076-0825/10/2/25.

[33] K. Aouali, N. Kacem, N. Bouhaddi, Functionalization of internal resonance in magnetically coupled resonators for highly efficient and wideband hybrid vibration energy harvesting, Sensors 22 (2022) 7657. doi:https://doi.org/10.3390/s22197657.

[34] S. Hermann, P. Butaud, R. de O. Teloli, J.-F. Manceau, M. Savary, G. Chevallier, Magnetically induced friction damping based on magnetoactive elastomers — a proof of concept, Journal of Sound and Vibration 534 (2022) 117000. URL: https://www.sciencedirect.com/science/article/pii/S0022460X2200222X. doi:10.1016/j.jsv.2022.117000.

[35] A. Barbosa, N. Kacem, N. Bouhaddi, A design methodology for nonlinear oscillator chains enabling energy localization tuning and soliton stability enhancement with optimal damping, Mechanical Systems and Signal Processing 213 (2024) 111358. doi:10.1016/j.ymssp.2024.111358.

[36] A. Barbosa, N. Kacem, N. Bouhaddi, Standing solitons tuned by impurities in damped nonlinear lattices under external excitation, Phys. Rev. Lett. 133 (2024) 187201. URL: https://link.aps.org/doi/10.1103/PhysRevLett.133.187201. doi:10.1103/PhysRevLett.133.187201.

[37] M. Farhan, A. G. Muthalif, M. S. M. Ali, Innovative approaches to optimize vibration energy harvesting (veh): A comprehensive review, Energy Reports 12 (2024) 5194–5219. doi:10.1016/j.egyr.2024.11.006.

[38] A. Moslemi, M. Rashidi, A. M. Nazar, P. Sharafi, Advancements in vibration-based energy harvesting systems for bridges: A literature and systematic review, Results in Engineering 26 (2025) 104622. doi:10.1016/j.rineng.2025.104622.

[39] L. Wang, Z. Fei, C. Duan, X. Han, M. Li, W. Gao, Y. Xia, C. Jia, Q. Lin, Y. Zhao, Z. Li, L. Zhao, Z. Jiang, R. Maeda, Self-sustained and self-wakeup wireless vibration sensors by electromagnetic-piezoelectric-triboelectric hybrid energy harvesting, Applied Energy 355 (2024) 122207. doi:10.1016/j.apenergy.2023.122207.

[40] S. N. Masabi, H. Fu, J. Flint, S. Theodossiades, A multi-stable rotational energy harvester for arbitrary bi-directional horizontal excitation at ultra-low frequencies for self-powered sensing, Smart Materials and Structures 33 (2024) 095017. doi:10.1088/1361-665x/ad649b.

[41] H. Xu, S. Zhou, Theoretical analysis and potential engineering application of an energy harvester, International Journal of Mechanical Sciences 275 (2024) 109284. doi:10.1016/j.ijmecsci.2024.109284.

[42] X. Fang, J. Lou, J. Wang, K.-C. Chuang, H. M. Wu, Z. L. Huang, A self-excited bistable oscillator with a light-powered liquid crystal elastomer, International Journal of Mechanical Sciences 271 (2024) 109124. doi:10.1016/j.ijmecsci.2024.109124.

[43] R. Sun, S. Zhou, Z. Li, L. Cheng, Dual electromagnetic mechanisms with internal resonance for ultra-low frequency vibration energy harvesting, Applied Energy 369 (2024) 123528. doi:10.1016/j.apenergy.2024.123528.

[44] S. Lee, D. Kang, Y. Je, W. Moon, Resonant frequency variations in a piezoelectric microcantilever sensor under varying operational conditions, Journal of Micromechanics and Microengineering 22 (2012) 105035. URL: https://dx.doi.org/10.1088/0960-1317/22/10/105035. doi:10.1088/0960-1317/22/10/105035.

[45] A. Wu, S. M. Mwachaka, Y. Pei, Q. Fu, A novel weak signal detection method of electromagnetic lwd based on a duffing oscillator, Journal of Sensors 2018 (2018) 5847081. doi:https://doi.org/10.1155/2018/5847081.

[46] K. Aledealat, K. Khasawinah, A. Obeidat, M. Gharaibeh, A. Jaradat, M. K. Hasan (Qaseer), A. A. Rousan, Sensitive detection schemes for small variations in the damping coefficient based on the duffing-holmes oscillator with a potential application in magnetic sensing, AIP Advances 8 (2018) 095102. doi:10.1063/1.5045496.

[47] H. Zhang, M. Pandit, G. Sobreviela, M. Parajuli, D. Chen, J. Sun, C. Zhao, A. A. Seshia, Mode-localized accelerometer in the nonlinear duffing regime with 75 ng bias instability and 95 ng/hz noise floor, Microsystems & Nanoengineering 8 (2022) 17. URL: https://doi.org/10.1038/s41378-021-00340-4. doi:10.1038/s41378-021-00340-4.

[48] F. Najar, M. Ghommem, A. Abdelkefi, A double-side electrically-actuated arch microbeam for pressure sensing applications, International Journal of Mechanical Sciences 178 (2020) 105624. URL: https://www.sciencedirect.com/science/article/pii/S0020740319340950. doi:10.1016/j.ijmecsci.2020.105624.

[49] Z. Liu, B. Qin, Z. Shi, X. Wang, Q. Lv, X. Wei, R. Huan, Nonlinearity-induced asymmetric synchronization region in micromechanical oscillators, Micromachines 15 (2024) 238. doi:10.3390/mi15020238.

[50] V.-N. Nguyen, S. Baguet, C.-H. Lamarque, R. Dufour, Bifurcation-based micro-/nanoelectromechanical mass detection, Nonlinear Dynamics 79 (2014) 647–662. doi:10.1007/s11071-014-1692-7.

[51] M. Shaat, A. Abdelkefi, Modeling the material structure and couple stress effects of nanocrystalline silicon beams for pull-in and bio-mass sensing applications, International Journal of Mechanical Sciences 101–102 (2015) 280–291. URL: https://www.sciencedirect.com/science/article/pii/S0020740315002817. doi:10.1016/j.ijmecsci.2015.08.002.

[52] R. Potekin, S. Kim, D. M. McFarland, L. A. Bergman, H. Cho, A. F. Vakakis, A micromechanical mass sensing method based on amplitude tracking within an ultra-wide broadband resonance, Nonlinear Dynamics 92 (2018) 287–304.

[53] J. Feng, H. Yu, Y. Li, W. Zhang, Nonlinear oscillation and detection sensitivity of clamped carbon nanotube mass sensor under thermal load, Composite Structures 323 (2023) 117444. URL: https://www.sciencedirect.com/science/article/pii/S0263822323007900. doi:https://doi.org/10.1016/j.compstruct.2023.117444.

[54] S. Azizi, H. Madinei, H. H. Khodaparast, S. Faroughi, M. I. Friswell, On the nonlinear dynamics of a piezoresistive based mass switch based on catastrophic bifurcation, International Journal of Mechanics and Materials in Design 19 (2023) 521–535. URL: https://doi.org/10.1007/s10999-023-09650-z. doi:10.1007/s10999-023-09650-z.

[55] D. Peng, Y. Zhang, Nonlinear dynamic behavior of single-layered black phosphorus with an attached mass, Materials Research Express 11 (2024) 065008. doi:10.1088/2053-1591/ad5815.

[56] Y. Mao, H. Dankowicz, On a principle for mass sensing using self-excited template dynamics of coupled oscillators and root-finding algorithms, Journal of Sound and Vibration 571 (2024) 118027. doi:10.1016/j.jsv.2023.118027.

[57] W. H. Waugh, B. J. Gallacher, J. S. Burdess, A high-sensitivity resonant sensor realized through the exploitation of nonlinear dynamic behaviour, Measurement Science and Technology 22 (2011) 105202. URL: https://dx.doi.org/10.1088/0957-0233/22/10/105202. doi:10.1088/0957-0233/22/10/105202.

[58] H. Han, J. Luo, L. Gao, Q. Deng, L. Zhao, X. Mu, A wideband vibration sensor with piecewise nonlinear and up-frequency coupling strategy for mechanical fault monitoring, Nano Energy 129 (2024) 110040. doi:10.1016/j.nanoen.2024.110040.

[59] P. Kudela, M. Radzienski, M. Miniaci, P. Fiborek, W. Ostachowicz, The design and testing of an ultrasensitive device with embedded phononic crystals for the detection and localisation of nonlinear guided waves, Journal of Sound and Vibration 611 (2025) 119155. doi:10.1016/j.jsv.2025.119155.

[60] L. Nsubuga, L. Duggen, F. Balzer, S. Høegh, T. L. Marcondes, W. Greenbank, H.-G. Rubahn, R. de Oliveira Hansen, Modeling nonlinear dynamics of functionalization layers: Enhancing gas sensor sensitivity for piezoelectrically driven microcantilever, ACS Sensors 9 (2024) 1842–1856. doi:10.1021/acssensors.3c02393.

[61] V. Gubbi, T. Ivanov, K. Ved, C. Lenk, M. Ziegler, Bio-inspired acoustic mems sensor with tunable resonance frequency, Sensors and Actuators A: Physical 387 (2025) 116369. doi:10.1016/j.sna.2025.116369.

[62] B. Torteman, Y. Kessler, A. Liberzon, S. Krylov, Micro-beam resonator parametrically excited by electro-thermal joule's heating and its use as

a flow sensor, Nonlinear Dynamics 98 (2019) 3051–3065. doi:10.1007/s11071-019-05031-4.

[63] C. Li, M. Zheng, K. Bi, W. Zhang, Y. Hong, H. Zhang, J. Miao, J. Xiong, A noncontact passive temperature-vibration multiparameter sensor, IEEE Sensors Journal 25 (2025) 5438–5445. doi:10.1109/jsen.2024.3520196.

[64] C. Liu, M. Shi, W. Zhang, Comparative study of six generic models for dual-objective vibration mitigation and energy harvesting, Engineering Structures 327 (2025) 119640. doi:10.1016/j.engstruct.2025.119640.

[65] L. Wang, W. Liu, X. Lin, Z. Yan, X. Nie, Study of vibration suppression and energy harvesting for a vibration-based piezoelectric–electromagnetic energy harvester with nonlinear energy sink, Journal of Magnetism and Magnetic Materials 602 (2024) 172200. doi:10.1016/j.jmmm.2024.172200.

[66] C. Xu, Y. Yang, C. H. Wang, L. Zhao, Simultaneous low-frequency vibration suppression and energy harvesting using a metastructure with alternately combined nonlinear local resonators, Mechanical Systems and Signal Processing 211 (2024) 111241. doi:10.1016/j.ymssp.2024.111241.

[67] H. Alimohammadi, K. Vassiljeva, S. H. HosseinNia, E. Petlenkov, Nonlinear dynamics in peh for enhanced power output and vibration suppression in metastructures, Nonlinear Dynamics 112 (2024) 12941–12963. doi:10.1007/s11071-024-09739-w.

[68] G. Sui, X. Shan, Y. Chen, C. Zhou, C. Hou, H. Li, T. Cheng, Dual-function of energy harvesting and vibration isolation via quasi-zero stiffness piezoelectric mechanism, Energy 301 (2024) 131711. doi:10.1016/j.energy.2024.131711.

[69] S. Fang, K. Chen, B. Zhao, Z. Lai, S. Zhou, W.-H. Liao, Simultaneous broadband vibration isolation and energy harvesting at low frequencies with quasi-zero stiffness and nonlinear monostability, Journal of Sound and Vibration 553 (2023) 117684. doi:10.1016/j.jsv.2023.117684.

[70] X. Huang, Exploiting multi-stiffness combination inspired absorbers for simultaneous energy harvesting and vibration mitigation, Applied Energy 364 (2024) 123124. doi:10.1016/j.apenergy.2024.123124.

[71] J.-J. Lu, G. Yan, W.-H. Qi, H. Yan, F.-R. Liu, T.-Y. Zhao, W.-M. Zhang, Integrated vibration isolation and actuation via dual nonlinear stiffness regulation, International Journal of Mechanical Sciences 263 (2024) 108760. doi:10.1016/j.ijmecsci.2023.108760.

[72] C. Xia, W. Zhang, J. Lang, J. Chen, Z. Zhao, L. Zhang, J. Song, Y. Xia, L. He, D. F. Wang, Z. Wang, Achieving transition between internal resonance and mode localization through coupling strength modulation, Journal of Sound and Vibration 589 (2024) 118575. doi:10.1016/j.jsv.2024.118575.

[73] M. Bian, Z. Xu, X. Tang, C. Chen, H. Jia, Tri-objective and multi-parameter geometric optimization of two-stage radioisotope thermoelectric generator based on nsga-ii, Applied Thermal Engineering 258 (2025) 124685. doi:10.1016/j.applthermaleng.2024.124685.

[74] H. H. Zhang, X. Y. Liu, Y. Liu, Z. C. Fan, H. L. Du, Thermal-mechanical-electromagnetic multiphysics simulation of satellite phased array antenna based on dgtd and fem method, IEEE Journal on Multiscale and Multiphysics Computational Techniques 9 (2024) 236–246. doi:10.1109/jmmct.2024.3428517.

[75] H. H. Zhang, Z. L. Jia, P. F. Zhang, Y. Liu, L. J. Jiang, D. Z. Ding, Electromagnetic-circuital-thermal-mechanical multiphysics numerical simulation method for microwave circuits, IEEE Journal on

Multiscale and Multiphysics Computational Techniques 9 (2024) 129–141. doi:10.1109/jmmct.2024.3372619.

[76] D. Luo, Z. Li, Y. Li, H. Zhang, X. Wang, A fully coupled thermal-fluid-electric-mechanics multiphysics numerical model for comprehensive performance evaluation of annular thermoelectric generators, Case Studies in Thermal Engineering 72 (2025) 106329. doi:10.1016/j.csite.2025.106329.

[77] W. Wei, X. Chen, Z. Zong, R. Qiao, Z. Shao, N. Ni, Study on the electromagnetic-thermal-mechanical coupling damage of concrete under microwave irradiation, Journal of Building Engineering 98 (2024) 111061. doi:10.1016/j.jobe.2024.111061.

[78] I. Sobianin, S. D. Psoma, A. Tourlidakis, A 3d-printed piezoelectric microdevice for human energy harvesting for wearable biosensors, Micromachines 15 (2024) 118. doi:10.3390/mi15010118.

[79] W. Zhang, G. Wang, Y. Guo, Research on damping and energy recovery characteristics of a novel mechanical-electrical-hydraulic regenerative suspension system, Energy 271 (2023) 127022. doi:10.1016/j.energy.2023.127022.

[80] A. Mondal, A. K. Gautam, N. Khare, Boosting electrical efficiency in hybrid energy harvesters by scavenging ambient thermal and mechanical energy, Energy Conversion and Management 332 (2025) 119739. URL: https://www.sciencedirect.com/science/article/pii/S0196890425002626. doi:https://doi.org/10.1016/j.enconman.2025.119739.

[81] I. A. Fadzallah, N. S. Sabran, M. M. I. M. Hasnan, T. Ono, M. F. M. Sabri, Computational modeling and theoretical analysis of polyvinylidene fluoride microarrays for hybrid piezo-pyroelectric energy harvest-

ing, Polymers for Advanced Technologies 35 (2024) e6419. doi:https://doi.org/10.1002/pat.6419.

[82] Y. Liang, Y.-S. Lin, Mems electrothermal actuator with highly linear actuation and stable characteristics, Materials Chemistry and Physics 341 (2025) 130967. doi:10.1016/j.matchemphys.2025.130967.

[83] R.-J. Xu, Y.-S. Lin, Actively mems-based tunable metamaterials for advanced and emerging applications, Electronics 11 (2022) 243. doi:10.3390/electronics11020243.

[84] S. Mohaidat, H. Nikfarjam, M. Fayad, S. Pourkamali, F. Alsaleem, Electrothermal bimorph mems sensor for helium detection, IEEE Sensors Journal 24 (2024) 31860–31866. doi:10.1109/JSEN.2024.3447278.

[85] I. Yotov, G. Todorov, T. Gavrilov, T. Todorov, Magnetic frequency tuning of a shape memory alloy thermoelectric vibration energy harvester, Energies 18 (2025). URL: https://www.mdpi.com/1996-1073/18/13/3341. doi:10.3390/en18133341.

[86] Z.-C. T. Shi-Rong Li, Y.-H. Zhou, Free vibration of heated euler–bernoulli beams with thermal postbuckling deformations, Journal of Thermal Stresses 27 (2004) 843–856. URL: https://doi.org/10.1080/01495730490486352. doi:10.1080/01495730490486352. arXiv:https://doi.org/10.1080/01495730490486352.

[87] L. C. Trinh, T. P. Vo, H.-T. Thai, T.-K. Nguyen, An analytical method for the vibration and buckling of functionally graded beams under mechanical and thermal loads, Composites Part B: Engineering 100 (2016) 152–163. URL: https://www.sciencedirect.com/science/article/pii/S1359836816302980. doi:https://doi.org/10.1016/j.compositesb.2016.06.067.

[88] R. Masana, M. F. Daqaq, Electromechanical Modeling and Nonlinear Analysis of Axially Loaded Energy Harvesters, Journal of Vibration and Acoustics 133 (2010) 011007. doi:10.1115/1.4002786.

[89] S. A. Emam, A. H. Nayfeh, On the nonlinear dynamics of a buckled beam subjected to a primary-resonance excitation, Nonlinear Dynamics 35 (2004) 1–17. URL: https://doi.org/10.1023/B:NODY.0000017466.71383.d5. doi:10.1023/B:NODY.0000017466.71383.d5.

[90] A. H. Nayfeh, S. A. Emam, Exact solution and stability of postbuckling configurations of beams, Nonlinear Dynamics 54 (2008) 395–408. URL: https://doi.org/10.1007/s11071-008-9338-2. doi:10.1007/s11071-008-9338-2.

[91] W.-P. Sun, W.-J. Su, Design and analysis of an extended buckled beam piezoelectric energy harvester subjected to different axial preload, Smart Materials and Structures 33 (2024) 055007. URL: https://dx.doi.org/10.1088/1361-665X/ad38a4. doi:10.1088/1361-665X/ad38a4.

[92] G. C. Kardarakos, N. A. Chrysochoidis, D. Varelis, D. A. Saravanos, Numerical and experimental investigation of the energy harvesting performance of electromechanically coupled piezoelectric prestressed beams subjected to nonlinear vibrations, Smart Materials and Structures 32 (2023) 035019. URL: https://dx.doi.org/10.1088/1361-665X/acb472. doi:10.1088/1361-665X/acb472.

[93] S. Osinaga, S. Machado, M. Febbo, An analytical model of the electromechanical coupling for a piezoelectric stepped buckled beam for energy harvesting applications, Mechanical Systems and Signal Processing 179 (2022) 109355. URL: https://www.sciencedirect.com/science/article/pii/S0888327022004885. doi:https://doi.org/10.1016/j.ymssp.2022.109355.

[94] R. Aloui, W. Larbi, M. Chouchane, Global sensitivity analysis of piezoelectric energy harvesters, Composite Structures 228 (2019) 111317. URL: https://www.sciencedirect.com/science/article/pii/S0263822319321038. doi:https://doi.org/10.1016/j.compstruct.2019.111317.

[95] R. Aloui, W. Larbi, M. Chouchane, Uncertainty quantification and global sensitivity analysis of piezoelectric energy harvesting using macro fiber composites, Smart Materials and Structures 29 (2020) 095014. URL: https://dx.doi.org/10.1088/1361-665X/ab9f12. doi:10.1088/1361-665X/ab9f12.

[96] Y. Wu, L. Li, Y. Fan, H. Ma, W. Wang, J.-L. Christen, M. Ichchou, Design of semi-active dry friction dampers for steady-state vibration: sensitivity analysis and experimental studies, Journal of Sound and Vibration 459 (2019) 114850. URL: https://www.sciencedirect.com/science/article/pii/S0022460X19304043. doi:https://doi.org/10.1016/j.jsv.2019.114850.

[97] R. O. Ruiz, V. Meruane, Uncertainties propagation and global sensitivity analysis of the frequency response function of piezoelectric energy harvesters, Smart Materials and Structures 26 (2017) 065003. URL: https://dx.doi.org/10.1088/1361-665X/aa6cf3. doi:10.1088/1361-665X/aa6cf3.

[98] V. M. d. S. Santos, Y. A. D. Martins, H. E. A. A. d. Santos, T. d. P. Sales, D. A. Rade, Stochastic modeling of periodic beams under uncertain boundary conditions and environmental fluctuations, International Journal of Mechanical Sciences 285 (2025) 109779. URL: https://www.sciencedirect.com/science/article/pii/S0020740324008208. doi:10.1016/j.ijmecsci.2024.109779.

[99] S. Leadenham, A. Erturk, M-shaped asymmetric nonlinear oscillator

for broadband vibration energy harvesting: Harmonic balance analysis and experimental validation, Journal of Sound and Vibration 333 (2014) 6209–6223. URL: https://www.sciencedirect.com/science/article/pii/S0022460X14005537. doi:https://doi.org/10.1016/j.jsv.2014.06.046.

[100] S. Zhao, U. Radhakrishna, J. H. Lang, Impact of duffing and piezoelectric-coupling nonlinearities on piezoelectric vibration energy harvesting, IEEE Sensors Journal 24 (2024) 8132–8141. doi:10.1109/JSEN.2024.3356664.

[101] M. Javani, M. R. Eslami, Y. Kiani, Active control of thermally induced vibrations of temperature-dependent fgm circular plate with piezoelectric sensor/actuator layers, Aerospace Science and Technology 146 (2024) 108997. doi:10.1016/j.ast.2024.108997.

[102] F. Abbaspour, H. Arvin, M. Shahriari-kahkeshi, Nonlinear vibration control of a piezoelectric graphene sheet reinforced microplate with thermal uncertainty: Feedback linearization and sliding mode approaches, Thin-Walled Structures 181 (2022) 110129. URL: https://www.sciencedirect.com/science/article/pii/S0263823122006814. doi:https://doi.org/10.1016/j.tws.2022.110129.

[103] N. Moustafa, R. Talebitooti, K. Daneshjou, Effect of thermal uncertainty on piezoelectric control of doubly curved bimorph shell: acoustic characteristics, Archive of Applied Mechanics 94 (2024) 2967–2987. doi:10.1007/s00419-024-02653-y.

[104] Y. Zhang, Y. Gao, S. Yang, X. Yue, Response analysis of asymmetric monostable energy harvester with an uncertain parameter, International Journal of Non-Linear Mechanics 163 (2024) 104752. URL: https://www.sciencedirect.com/science/

article/pii/S0020746224001173. doi:https://doi.org/10.1016/j.ijnonlinmec.2024.104752.

[105] R. A. Borges, L. F. Rodovalho, T. de P. Sales, D. A. Rade, Stochastic eigenfrequency and buckling analyses of plates subjected to random temperature distributions, Mechanical Systems and Signal Processing 147 (2021) 107088. URL: https://www.sciencedirect.com/science/article/pii/S088832702030474X. doi:https://doi.org/10.1016/j.ymssp.2020.107088.

[106] S. Sharma, S. Sen, Bridge damage detection in presence of varying temperature using two-step neural network approach, Journal of Bridge Engineering 26 (2021) 04021027.

[107] A. Erturk, D. J. Inman, A distributed parameter electromechanical model for cantilevered piezoelectric energy harvesters, Journal of Vibration and Acoustics 130 (2008) 041002. URL: https://doi.org/10.1115/1.2890402. doi:10.1115/1.2890402.

[108] C. Touzé, A. Vizzaccaro, O. Thomas, Model order reduction methods for geometrically nonlinear structures: a review of nonlinear techniques, Nonlinear Dynamics 105 (2021) 1141–1190. doi:10.1007/s11071-021-06693-9.

[109] A. Deraemaeker, H. Nasser, A. Benjeddou, A. Preumont, Mixing rules for the piezoelectric properties of macro fiber composites, Journal of Intelligent Material Systems and Structures - J INTEL MAT SYST STRUCT 20 (2009) 1475–1482. doi:10.1177/1045389X09335615.

[110] M. A. Attia, S. A. Mohamed, Nonlinear thermal buckling and postbuckling analysis of bidirectional functionally graded tapered microbeams based on reddy beam theory, Engineering with Computers 38 (2020) 525–554. doi:10.1007/s00366-020-01080-1.

[111] M. Derakhshani, N. Momenzadeh, T. A. Berfield, Analytical and experimental study of a clamped-clamped, bistable buckled beam low-frequency pvdf vibration energy harvester, Journal of Sound and Vibration 497 (2021) 115937. doi:10.1016/j.jsv.2021.115937.

[112] Z. P. Bažant, L. Cedolin, Stability of structures: elastic, inelastic, fracture, and damage theories, Courier Corporation, 2003.

[113] M. R. Eslami, R. B. Hetnarski, J. Ignaczak, N. Noda, N. Sumi, Y. Tanigawa, Theory of elasticity and thermal stresses, volume 197, Springer, 2013.

[114] R. de O. Teloli, P. Butaud, G. Chevallier, S. da Silva, Good practices for designing and experimental testing of dynamically excited jointed structures: The orion beam, Mechanical Systems and Signal Processing 163 (2022) 108172. URL: https://www.sciencedirect.com/science/article/pii/S0888327021005495. doi:https://doi.org/10.1016/j.ymssp.2021.108172.

[115] M. Bonnin, F. L. Traversa, F. Bonani, An impedance matching solution to increase the harvested power and efficiency of nonlinear piezoelectric energy harvesters, Energies 15 (2022) 2764.

[116] G. Xia, S. Zhang, X. Kang, T. Han, L. Chen, C. Lim, Performance analysis of nonlinear piezoelectric energy harvesting system under bidirectional excitations, Composite Structures 324 (2023) 117529.

[117] Z. Yang, A. Erturk, J. Zu, On the efficiency of piezoelectric energy harvesters, Extreme Mechanics Letters 15 (2017) 26–37.

[118] W. Wang, J. Cao, C. R. Bowen, S. Zhou, J. Lin, Optimum resistance analysis and experimental verification of nonlinear piezoelectric energy harvesting from human motions, Energy 118 (2017) 221–230.

[119] S. Bae, P. Kim, Load resistance optimization of a broadband bistable piezoelectric energy harvester for primary harmonic and subharmonic behaviors, Sustainability 13 (2021) 2865.